Optical Properties Using Adaptive Selection of NIR/SWIR Reflectance Correction and Quasi-Analytic Algorithms for the MODIS-Aqua in Estuarine-Ocean Continuum: Application to the Northern Gulf of Mexico

Ishan D. Joshi and Eurico J. D'Sa

Abstract—An adaptive selection of the near/shortwave infrared (NIR/SWIR) reflectance correction and the quasi-analytic algorithms (QAAs) is proposed for the Moderate Resolution Imaging Spectroradiometer (MODIS-Aqua) to utilize the strengths of different correction algorithms and QAAs in a single satellite scene with water types ranging from turbid coastal to clear open ocean waters. A blended satellite product is generated by merging three atmospheric-correction algorithms (AD-ATCOR): 1) iterative NIR correction; 2) management unit of the north sea mathematical models (MUMM); and 3) SWIR, using a spectral threshold-based selection for different water types. The validation analysis of a blended remote sensing reflectance product showed overall good agreement with AERONET-OC observations followed by NASA bio-optical marine algorithm data set (NOMAD) at the blue wavelengths and the estuarine data set at the green and red wavelengths. The results suggest that the adaptive method is a better alternative to address the challenging problem of selecting different correction algorithms for different water types in a single satellite scene. Likewise, an adaptive selection of a QAA (AD-QAA) used the QAA-v5 and the QAA-V to obtain merged inherent optical property (IOP) products in a single MODIS-Aqua scene with varying water types. As a case study, the two adaptive selection procedures were sequentially applied to the MODIS-Aqua imagery representing four environmental conditions in the northern Gulf of Mexico. Improved retrievals of the total absorption and backscattering coefficients along an estuarine to ocean continuum demonstrated the effectiveness of this method in an optically complex and dynamic river-dominated system.

Index Terms—Atmospheric-correction algorithm, Moderate Resolution Imaging Spectroradiometer (MODIS-Aqua), northern Gulf of Mexico (nGoM), quasi-analytic algorithm (QAA).

Ishan D. Joshi is with the Scripps Institution of Oceanography, University of California at San Diego, San Diego, CA 92093 USA (e-mail: isjoshi@ucsd.edu).

Eurico J. D'Sa is with the Department of Oceanography and Coastal Sciences, Louisiana State University, Baton Rouge, LA 70803 USA (e-mail: ejdsa@lsu.edu).

I. INTRODUCTION

BIOGEOCHEMICAL water constituents, such as phytoplankton, mineral particles, and colored dissolved organic matter (CDOM), play important roles in marine biogeochemical cycles and can be directly or indirectly linked to various local and global phenomena such as harmful algal blooms, pollutant transport, and climate change [1]–[5]. Therefore, regular monitoring of such ecologically important variables is of primary interest for various national and international organizations and the scientific community to help resource management and public safety decisions. As these water constituents interact with the light field, their inherent optical properties (IOPs) such as absorption and backscattering coefficients can be used as proxies for their abundance in the aquatic medium [6]–[9]. Traditional approaches of measuring IOPs and mass concentrations in the field or laboratory settings are time consuming and largely limited by their spatial and temporal coverage. However, since the launch of the first ocean color satellite, the Coastal Zone Color Scanner (CZCS), satellite remote sensing has served as an attractive alternative to the traditional methods and has continuously evolved to provide more reliable ocean color products due to improved spectral and radiometric capabilities in subsequent satellite sensors [e.g., Sea-viewing Wide Field of view Sensor (SeaWiFS), Moderate Resolution Imaging Spectroradiometer (MODIS-Aqua), Medium Resolution Imaging Spectroradiometer (MERIS), Visible and Infrared Imaging Radiometric Suite (VIIRS), and recently, Ocean and Land Color Instrument (Sentinel-3 OLCI)] [10], [11].

Nevertheless, the use of satellites to monitor ocean color comes with a challenging task of removing the contributions from atmospheric gases and aerosols to the total light sensed by a satellite sensor at the top-of-the-atmosphere (TOA) (also known as the atmospheric-correction process) [12]. The atmospheric-correction process is a vital step to obtain reasonable estimates of the normalized water-leaving radiance ($nL_w(\lambda)$, radiance normalized to hypothetical conditions of the Sun at zenith and no atmosphere [13]) and subsequently to gain confidence on satellite-derived

ocean color products (e.g., $a_{tnw}(\lambda)$—total nonwater absorption coefficient, $b_{bp}(\lambda)$—particle backscattering coefficient). The first atmospheric-correction approach used two near-infrared (NIR) bands (e.g., 765 and 865 nm for SeaWiFS) and an assumption of negligible water-leaving radiance ($nL_w \approx 0$; commonly known as "black-pixel assumption" and "GW94") [14]. With this assumption, any signal in the NIR that is observed by a satellite sensor can be entirely considered due to the atmosphere and sea surface reflectance. The black-pixel assumption is generally valid in clear waters, where seawater is the dominant light absorber in the NIR and the optical properties are generally governed by phytoplankton and covarying water constituents. However, the use of black-pixel assumption degrades and often fails toward particle-rich turbid waters where higher particle concentrations substantially contribute to the total backscattering signal and, thus, to nonnegligible reflectance in the NIR; as such, numerous NIR-based ocean reflectance correction algorithms have been proposed with the consideration of nonzero water-leaving radiance in the NIR [15]–[21]. However, the application and success of these algorithms vary significantly based on underlying assumptions, water types, and region of interest. For example, the iterative NIR-correction algorithm by Bailey *et al.* [20] (initially developed by Stumpf *et al.* [17]) is based on the GW94 [14] and bio-optical models and has been performing well in chlorophyll-a (Chl-a) -dominated waters (e.g., productive shelf waters and open ocean) [9], [22], [23]. In contrast, the management unit of the north sea mathematical models (MUMM) NIR-correction algorithm by Ruddick *et al.* [16], [24] is based on an assumption of spatial homogeneity of the ratio of any two NIR water-leaving reflectance and aerosol reflectance over a region of interest; this method is known to show a better performance in moderately turbid sediment-rich waters [23]. Likewise, the short-wave infrared (SWIR) correction algorithm by Wang and Shi [18] is the GW94 but uses two SWIR wavelengths instead of NIR; it has demonstrated its efficacy in highly turbid waters with the assumption of zero water-leaving radiance in the SWIR region in highly reflecting waters due to strong water absorption [19], [25], [26]. Although these correction algorithms have provided reasonable estimates of ocean color products in a variety of water types throughout the world, their application is limited to a subset of satellite imagery and often fail to perform satisfactorily and consistently in waters with varying color changes—from brown (e.g., turbid estuarine) to green (e.g., productive nearshore) and onto blue (e.g., clear open ocean) waters. To our knowledge, very few studies have worked toward merging the NIR and SWIR correction algorithms to provide a blended satellite product using thresholds either based on water turbidity or remote sensing reflectance [19], [27], [38]. However, the performance of such numerical thresholds often degrade in dynamic regions where the optical signature of surface water changes rapidly under the forcing of currents, winds, and river plumes.

To obtain reasonable estimates of IOPs, nL_w (or Rrs—remote sensing reflectance) needs to be linked to the in-water IOPs generally using mathematical formulations (e.g., empirical and semi-analytic models). A multiband quasi-analytic

algorithm (QAA) was developed to bypass major limitations of empirical and semi-analytical models in optically deep waters [28]. Subsequently, it has been improved as QAA-v5 for better performance in coastal waters [29]. The QAA-v5 has been evaluated in a variety of waters ranging from turbid inland waters to high-latitude oceans with an acceptable performance in coastal and oceanic waters but with decreasing accuracy toward CDOM-rich and sediment-rich estuarine and inland waters [29]–[35]. An empirical component was added to QAA-v6 to improve QAA's performance in turbid waters using a threshold (Rrs670 > 0.0015 sr^{-1}). This empirical component uses Rrs at the blue (B) and red (R) wavelengths and, thus, may not be an efficient choice for optically complex estuaries where the atmospheric-corrected blue bands often suffer from large uncertainties [22], [23]. Recently, Joshi and D'Sa [36] proposed the use of green (G) and red (R) wavelengths in the QAA especially for estuarine and nearshore waters (named as QAA-V) that showed the G-R model to perform better than the B-R model of QAA-v6 in turbid coastal waters.

In this study, we first demonstrate an approach to merge three commonly used variants of the GW94-based atmospheric correction algorithms, namely: 1) iterative NIR correction (BFW10); 2) MUMM NIR correction (R00); and 3) SWIR correction (WS05), using an adaptive selection of these algorithms based on spectral thresholds optimized for different water types for the MODIS-Aqua sensor. This was necessary to achieve the major objective of obtaining surface water IOPs in an entire satellite scene. We extend the previous work of Joshi and D'Sa [36] by blending the QAA-V with the standard QAA (QAA-v5) to enhance its capability to provide more accurate IOPs (e.g., a_{tnw} and b_{bp}) in the estuarine to open ocean transition zone in a satellite scene. The candidate NIR-correction and SWIR-correction and QAAs are first briefly described. Next, adaptive procedures for selecting the NIR/SWIR correction algorithms and the QAAs (AD-QAA) are described in detail and evaluated for the optically complex waters of the northern Gulf of Mexico (nGoM) using AERONET-OC observations and the MODIS-Aqua imagery. The adaptive selection of atmospheric correction algorithm (AD-ATCOR) and AD-QAA methodologies are also assessed on a subset of NASA bio-optical marine algorithm data set (NOMAD) and the estuarine data sets to investigate their applicability to various estuarine-coastal-oceanic transition regions. Finally, the performance of AD-ATCOR and AD-QAA is evaluated under different environmental conditions in the nGoM.

II. Candidate Algorithms

A. NIR- and SWIR-Correction Algorithms

Two NIR correction algorithms (BFW10 and R00) and one SWIR correction algorithm (WS05) are used to create a blended Rrs product; these three algorithms are based on a standard NIR atmospheric correction algorithm first developed by the GW94 and, thus, can be seen as an extension of the GW94 in turbid waters where the black-pixel assumption often fails.

The signal received at the TOA comprised several terms [37]

$$L_T(\lambda) = L_{ATM}(\lambda) + L_{SURF}(\lambda) + t_v L_w(\lambda) \qquad (1)$$

where $L_T(\lambda)$ is the total radiance received at the TOA which contains a contribution of atmospheric scattering $[L_{\text{ATM}}(\lambda)]$, a contribution of radiance reflected from the water surface $[L_{\text{SURF}}(\lambda)]$, and a part of water-leaving radiance $[L_w(\lambda)]$ reaching at the TOA. $L_{\text{ATM}}(\lambda)$ is composed of Rayleigh-scattering by gas molecules, aerosol scattering, and multiple scattering by gases and aerosols. $L_{\text{SURF}}(\lambda)$ represents contributions by Sun glint and sky radiance from the water surface and light reflected from white caps and foam. t_v is diffuse transmittance from sea to sensor at TOA. The ultimate goal of the atmospheric-correction process is to obtain more accurate estimates of $L_w(\lambda)$ from $L_T(\lambda)$ after the removal of surface reflectance and the atmosphere. Remote sensing reflectance is given by $\text{Rrs} = L_w(\lambda)/E_d(\lambda)$, where $E_d(\lambda)$ is the irradiance at the surface.

BFW10 algorithm was initially developed by Stumpf *et al.* [17] and later modified by Bailey *et al.* [20]. It is based on the standard GW94 algorithm [14] but uses an iterative method with bio-optical models to estimate L_w at the NIR wavelengths. The process begins with the GW94 by applying the black-pixel assumption to Rayleigh-corrected reflectance at two NIR wavelengths (e.g., water-leaving reflectance $\rho_w \approx 0$ at 748 and 869 nm for the MODIS-Aqua) to get the first guess of $\rho_w(\lambda)$. Next, ρ_w at 443, 488, and 547 are then used in the MODIS Chl-a OC3 algorithm to estimate concentrations of Chl-a at each pixel [39]. The Chl-a is subsequently fed to an empirical bio-optical model to get the absorption coefficient of CDOM and particles at the red wavelength $[a_{\text{dg}}(\text{Red})]$, which is then combined with known water absorption $[a_w(\text{Red})]$ to obtain the total absorption coefficient at the red wavelength $[a_t(\text{Red})]$. Furthermore, $\rho_w(\text{Red})$ is converted to rrs(Red) (remote sensing reflectance just below the surface), which is then used together with $a_t(\text{Red})$ and $a_w(\text{Red})$ to get particulate backscattering coefficient at the red wavelength $(b_{\text{bp}}(\text{Red}))$. Next, assuming a power-law dependence of $b_{\text{bp}}(\lambda)$, $b_{\text{bp}}(\text{NIR})$ can be estimated from the $b_{\text{bp}}(\text{Red})$. Then, new estimates of ρ_w at two NIR wavelengths are obtained with available $b_{\text{bp}}(\text{NIR})$ and rrs(NIR) with an assumption of negligible $a_{\text{dg}}(\text{NIR})$. The estimated ρ_w at two NIR wavelengths are then removed from Rayleigh-corrected reflectance to get a new guess of $\rho_w(\lambda)$. This process is continued until $\rho_w(\text{Red})$ changes with less than 2% or maximum iteration is reached. A default value of maximum iteration limit is set to 10 for global data processing. However, this limit is configurable and can be investigated for other regions where ten iterations may not be sufficient for the convergence. The majority of our validation measurements were from low to moderately turbid coastal and estuarine waters where a default value (10 in this study) was sufficient to achieve the convergence of $\rho_w(\text{Red})$. Because the MODIS Chl-a OC3 algorithm and the Chl-a-based bio-optical model are crucial components of this algorithm, several studies have shown an excellent performance in Chl-a-dominated coastal and oceanic waters where the OC3 algorithm provides reasonable estimates of Chl-a. However, in particle-rich moderate to highly turbid waters, particulate backscattering itself shows high values of $\rho_w(\text{NIR})$ which violates the NIR black-pixel assumption, thus

leading to the maximum iteration limit before convergence and often results in saturation of the NIR bands and data dropouts [27].

The second NIR-correction algorithm, R00 (or MUMM; [16], [24]), also considers nonnegligible NIR water-leaving reflectance; however, in contrast to the BFW10, it is based upon two assumptions: 1) the shape of $\rho_w(\lambda)$ can be considered invariant in the NIR region due to strong water absorption, whereas the backscattering coefficient is spectrally independent over the NIR region. Hence, a ratio of ρ_w at two NIR wavelengths (α) is approximately constant and has a value of 1.945 for the MODIS-Aqua; and 2) the atmospheric composition does not significantly vary over a small region of interest and hence, the ratio of aerosol reflectance (ρ_{ATM}) at two NIR wavelengths (ϵ) can be considered as a fixed value that can be used for an entire region of interest. The R00 correction begins with the standard GW94 algorithm to obtain a scatter plot of Rayleigh-corrected reflectance $[\rho_{\text{rc}}(\lambda)]$ at two NIR wavelengths (e.g., 748 and 869 nm for MODIS-Aqua). A clear-water pixel is detected by a threshold of $0 < \rho_{\text{rc}}(\text{NIR}) < 0.015$. In a clear water pixel, $\rho_w(\text{NIR})$ can be taken as zero (the black-pixel assumption) and ϵ can be estimated from Rayleigh-corrected reflectance $(\rho_{\text{rc}} \approx \rho_{\text{ATM}})$ using two NIR wavelengths. Based on the second assumption, the estimated ϵ can be used for the entire scene with a fixed α and pixel specific $\rho_{\text{rc}}(\lambda)$ to obtain $\rho_{\text{ATM}}(\text{NIR})$ along with an appropriate aerosol model for the region. Lastly, the GW94 is run again with the new aerosol model. The R00 algorithm is more appropriate for moderately turbid waters as it relies on a constant water-leaving reflectance ratio at NIR wavelengths.

Wang and Shi [18] recommended using two SWIR bands (i.e., 1240 and 2130 nm for the MODIS-Aqua) in the GW94 algorithm for highly turbid waters where the black-pixel assumption fails for $\rho_w(\text{NIR})$. An underlying assumption for the WS05 is that the ocean is usually black in the SWIR region even in turbid waters due to much stronger water absorption, as much as 2–3 times higher than in the NIR [26]. Therefore, $\rho_w(\text{SWIR})$ can conceptually be considered as zero and the SWIR bands can be used instead of the NIR bands for selecting an aerosol model in the standard GW94 correction algorithm. Numerous studies have demonstrated improvement in estimating the water-leaving radiance with the WS05 in highly turbid environments [25], [40].

Recently, Goyens *et al.* [41] suggested to use a polynomial NIR relationship instead of a constant NIR ratio in MUMM NIR-correction and to constrain the BFW10 NIR-correction with spectral bounding relationships to improve the performance of these correction algorithms in turbid waters. Jiang and Wang [38] also suggested an improvement to the individual NIR-correction algorithms and proposed a blended NIR-correction algorithm [Bailey–MUMM–Wang (BMW) algorithm]. The BMW algorithm demonstrated its comparable performance to the SWIR-correction algorithm in turbid coastal and inland waters [38] and has been implemented in NOAA's MSL12 ocean processing system. The performance of the individual correction algorithm can be improved by implementing these modifications to their core structures. However, such a detailed analysis is beyond the scope of

this study. The blending approach of this study uses NIR and SWIR correction algorithms that are readily available in NASA's SeaDAS l2gen ocean color processing system to achieve the goal of obtaining improved estimates of the optical properties in heterogeneous waters in a satellite scene.

B. Quasi-Analytic Algorithms

Two multiband QAAs, QAA-v5 [28] and QAA-V [36], are used to obtain the IOPs (i.e., total nonwater absorption, $a_{\text{tnw}}(\lambda)$, and particulate backscattering, $b_{\text{bp}}(\lambda)$ coefficients) from a blended MODIS-Aqua Rrs image. The QAA methodology for the QAA-v5 and the QAA-V is mostly similar, except that the standard QAA-v5 uses a combination of two blue bands (e.g., 443 and 488 nm for the MODIS-Aqua) in the primary step of estimating the total nonwater absorption at a reference wavelength [28]

$$a_{\text{tnw}}555 = 10^{\left(-1.146 - 1.366 \times \ x - 0.469 \times x^2\right)}$$

where

$$x = \log_{10}\left(\frac{\text{rrs}443 + \text{rrs}488}{\text{rrs}555 + 5 \times \text{rrs}670 \times \frac{\text{rrs}670}{\text{rrs}488}}\right). \quad (2)$$

In estuarine and near-shore waters, the blue bands suffer large errors due to uncertainties in atmospheric correction, especially in coastal waters where high concentration of dissolved and inorganic particulate materials is often observed; hence, the use of such bands may not be ideal in optically complex waters. Additionally, the empirical relationships in the QAA-v5 were developed using NOMAD (https://seabass.gsfc.nasa.gov/wiki/NOMAD)—a database that is mostly skewed toward the coastal and oceanic environments; hence, the model coefficients may not be suitable for estuarine and near-shore environments. In contrast, the QAA-V was formulated using threshold-based empirical models that use a green to red band ratio to estimate $a_{\text{tnw}}555$. This algorithm, which was optimized using a suite of synthetic and *in situ* estuarine data sets, showed an improved performance in estuarine and near-shore waters as compared to the standard QAA. Detailed information on the QAA-v5 and the QAA-V can be obtained in [28] and [36].

III. DATA AND METHODOLOGY

A. Field Observations

The blending of three NIR/SWIR correction algorithms in a satellite scene is demonstrated first for the river-dominated region of the nGoM to show limitations associated with the application of each correction algorithm in an optically complex and dynamic region. The nGoM (Louisiana–Texas shelf) receives >90% of freshwater and nutrients via two large river systems, namely the Mississippi River (MR) and the Atchafalaya River (AR), and the region is known to experience strong east-to-west surface currents in nonsummer months [42]. The nGoM is well known for the summer hypoxia associated with high levels of river nutrient loading and primary production [43]. Another reason for choosing this region is the presence of NASA's aerosol robotic network
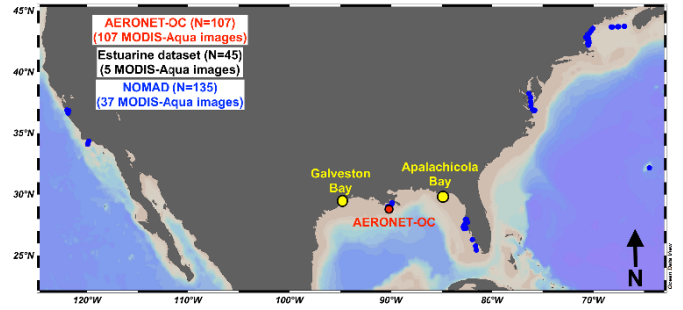

Fig. 1. Locations of field observations corresponding to three data sets: AERONET-OC—red, NOMAD—blue, the estuarine data set—yellow (Apalachicola Bay and Galveston Bay).

(AERONET-OC) site located to the south of Terrebonne Bay on the Louisiana shelf (see Fig. 1) [44], [45]; a total of 107 field matchups were obtained at the AERONET station corresponding to the MODIS-Aqua images (2011-2016) (https://aeronet.gsfc.nasa.gov/new_web/photo_db_v3/ WaveCIS_Site_CSI_6.html).

Field observations ($N = 45$; 5 MODIS-Aqua images) representing the estuarine environment were also obtained in Apalachicola Bay, USA (2015–2016) and Galveston Bay, USA (2017) and used to evaluate the adaptive selection approach in the relatively turbid and CDOM-rich waters of the nGoM. For the NOMAD (v2a) data set, MODIS-Aqua matchups were selected based on a time difference between field measurement and MODIS-Aqua overpass of $< \pm 3$ h and imagery that was cloud free and with no sunglint. Thus, clear-sky MODIS-Aqua matchups ($N = 135$; 37 MODIS-Aqua images) were used from the NOMAD data set to investigate the applicability of this approach (AD-ATCOR and AD-QAA) in different other coastal transition regions [47] (see Fig. 1).

B. Satellite Image Processing and Matchup Analysis

The MODIS Level-1A imagery was downloaded from the Ocean Color website maintained by NASA Ocean Biology Processing Group (https://oceancolor.gsfc.nasa.gov/) and processed to Level 2 using the l2gen module in SeaDAS 7.5 software (https://seadas.gsfc.nasa.gov/). Each Level 1A image was corrected for the atmosphere using three candidate algorithms: 1) BFW10 (l2gen parameters: aer_opt = −3, aer_wave_short = 748 nm, aer_wave_long = 869 nm); 2) R00 (l2gen parameters: aer_opt = −10, aer_wave_short = 748 nm, aer_wave_long = 869 nm); and 3) SWIR (l2gen parameters: aer_opt = −1, aer_wave_short = 1240 nm, aer_wave_long = 2130 nm). The NIR and SWIR bands were smoothed by a 3 × 3 pixel filter prior to using in the atmospheric-correction procedure in order to reduce the data loss due to detector issues and propagation of the salt–pepper effect of SWIR bands [low signal to noise ratio (SNR)] to other bands. This can be achieved by adding lines for the NIR and SWIR bands (i.e., ltrmean, 11, 3, 3, 1; ltrmean, 13, 3, 3, 1; ltrmean, 14, 3, 3, 1; and ltrmean, 16, 3, 3, 1) in a custom msl12_filter.dat file. The "ltrmean" represents averaging over Rayleigh-corrected radiance at the TOA.

The mask for high radiance at a sensor (HILT mask) was disabled. The SWIR band (2130 nm) was chosen for masking clouds using a threshold of 0.018 [48]. Three NIR- and SWIR-corrected MODIS-Aqua images (i.e., BFW10 image, R00 image, and WS05 image) were then reprojected using SeaDAS 7.5 reprojection tool and saved for further analysis in MATLAB. Recently, Aurin *et al.* [27] suggested the optimal spatial resolution requirement for detecting interpixel ocean color variability for different environments (e.g., ~500 m for the plume region, ~650 m for the near-shore region, and ~750 m for the shelf region, and ~1500 m for the off-shore region). Because this study includes all these regions, we chose a 500-m spatial resolution for the MODIS-Aqua imagery. For field-satellite matchup analysis, we have used the mean of 3×3-pixel box centered on a field station after applying a spatial homogeneity criterion, i.e., valid data if the coefficient of variation within a pixel box is less than 20% [49].

The time differences between AERONET-OC measurements and satellite overpass were kept as small as possible (i.e., mean = 30 min, standard deviation = 37 min, minimum = 0 min, and maximum = 153 min). It is worth noting that AERONET-OC multispectral instruments' spectral channels are slightly different than the MODIS-Aqua channels. In the absence of hyperspectral measurements and the relative spectral response (RSR) for the AERONET instruments, we have not considered the spectral band adjustment techniques [36], [46] and used a linear interpolation for the AERONET-OC data for minimizing spectral differences in matchup analysis.

C. AD-ATCOR and AD-QAA

To utilize the strengths of three well-known NIR- and SWIR-correction algorithms and two QAAs in a single satellite scene in which water type varies from turbid coastal to clear open ocean waters, we propose a methodology for a pixel-by-pixel selection of the reflectance correction algorithm based on the spectral criteria of different water types and for blending two QAAs, QAA-v5, and QAA-V, for the MODIS-Aqua. We chose the MODIS-Aqua from the current suite of sensors due to availability of the long historical record (2002-present) and relatively better spectral resolution suitable for developing the spectral criteria for the AD-ATCOR. The processing pathway of the AD-ATCOR and the AD-QAA is demonstrated in Fig. 2 which is summarized as follows.

The process begins with a BFW10-corrected image and the pixels of this image will be replaced with the corresponding pixels in the R00- and WS05-corrected images based on the following spectral criteria (see Fig. 2).

Step-1: In the BFW10 image.

Criterion 1: If Rrs667 > Rrs443, then a pixel is a turbid water pixel that will be replaced with a corresponding pixel in the R00 image. Criterion 2 is then applied to this modified image.

Criterion 2: If Rrs645 > Rrs555, then a pixel is highly turbid water pixel that will be replaced with a corresponding pixel in the WS05 image.

Criterion 3 (OPTIONAL): It detects the presence of the bright waters. Although these relatively brighter waters have been associated with coccolithophore blooms, previous studies have shown that resuspension of diatom frustules and fragments in combination with coccoliths could also contribute to sea surface brightness observed in field conditions or in satellite images [50], [51]. Thus, in a pixel if $[\max(\text{Rrs}(\lambda)) = (\text{Rrs488 OR Rrs531})$ and $(\text{Rrs678} - \text{Rrs667})/\text{Rrs667} \leq 0.05]$, then replace it with a corresponding pixel in the R00 image. This criterion is included to account for the presence of features previously associated with coccolithophores in surface waters and to support future *in situ* validation of satellite imagery.

Step-1: This step provides a blended Rrs image with all three ocean reflectance correction algorithms applied based on the aforementioned criteria. The atmospheric-corrected optimized Rrs image can now be used to derive IOPs (total absorption and particulate backscattering coefficients) using the AD-QAA.

Steps 2–4: These steps relate to the AD-QAA procedure and are similar to the standard QAA processing modules for the QAA-v5 and the QAA-V to obtain $\text{rrs}(\lambda)$, a green to red band ratio (ρ), and spectrally dependent backscattering to absorption ratio $u(\lambda)$ using the $\text{Rrs}(\lambda)$ image (from step-1) (see [29], [36]).

Step-5: This step blends two QAAs based on a threshold ρ_v (green to red band ratio from the QAA-V) (see [36, Fig. 3(b)]). To estimate $a_{\text{tnw}}555$, the AD-QAA uses two empirical models of QAA-V, one for a value of ρ_v less than 0.25 and another for $0.25 \geq \rho_v < 0.65$ as suggested in [36]. In contrast, it uses an empirical model of QAA-v5 for $\rho_v \geq 0.75$, mostly representing the clear open ocean; however, in the transition zone $(0.65 \geq \rho_v < 0.75)$, the AD-QAA takes an average of empirically derived $a_{\text{tnw}}555$ from the QAA-V and the QAA-v5 (see Fig. 2).

Steps 6–9: These steps are again similar to the standard QAA procedure for obtaining $b_{\text{bp}}(555)$ and the total-backscattering coefficient $b_{\text{bt}}(\lambda)$, and the total absorption coefficient $a_t(\lambda)$ (see Fig. 2). The major difference between the standard QAA-v5 and QAA-V is the use of different models for a power-law exponent (η), where the former uses an empirical relationship formulated using NOMAD, while the latter uses an empirical algorithm formulated in particle-rich waters around the MR plume [57]. At step-7, the AD-QAA uses QAA-V's η model for pixels with $\rho_v < 0.25$ and QAA-v5's η model for pixels with $\rho_v \geq 0.25$.

IV. RESULTS AND DISCUSSION

A. nGoM—An Optically Complex Coastal Region for Ocean Color Remote Sensing

The nGoM (Louisiana–Texas shelf) receives most of its freshwater and nutrients via two large rivers, MR and AR. A recent study suggested that the riverine nitrogen input accounts for ~80% of the total nitrogen loading on this shelf [42], making the MR–AR system as the dominant source of nutrients that support significant primary production that consequently fuels the world's second largest

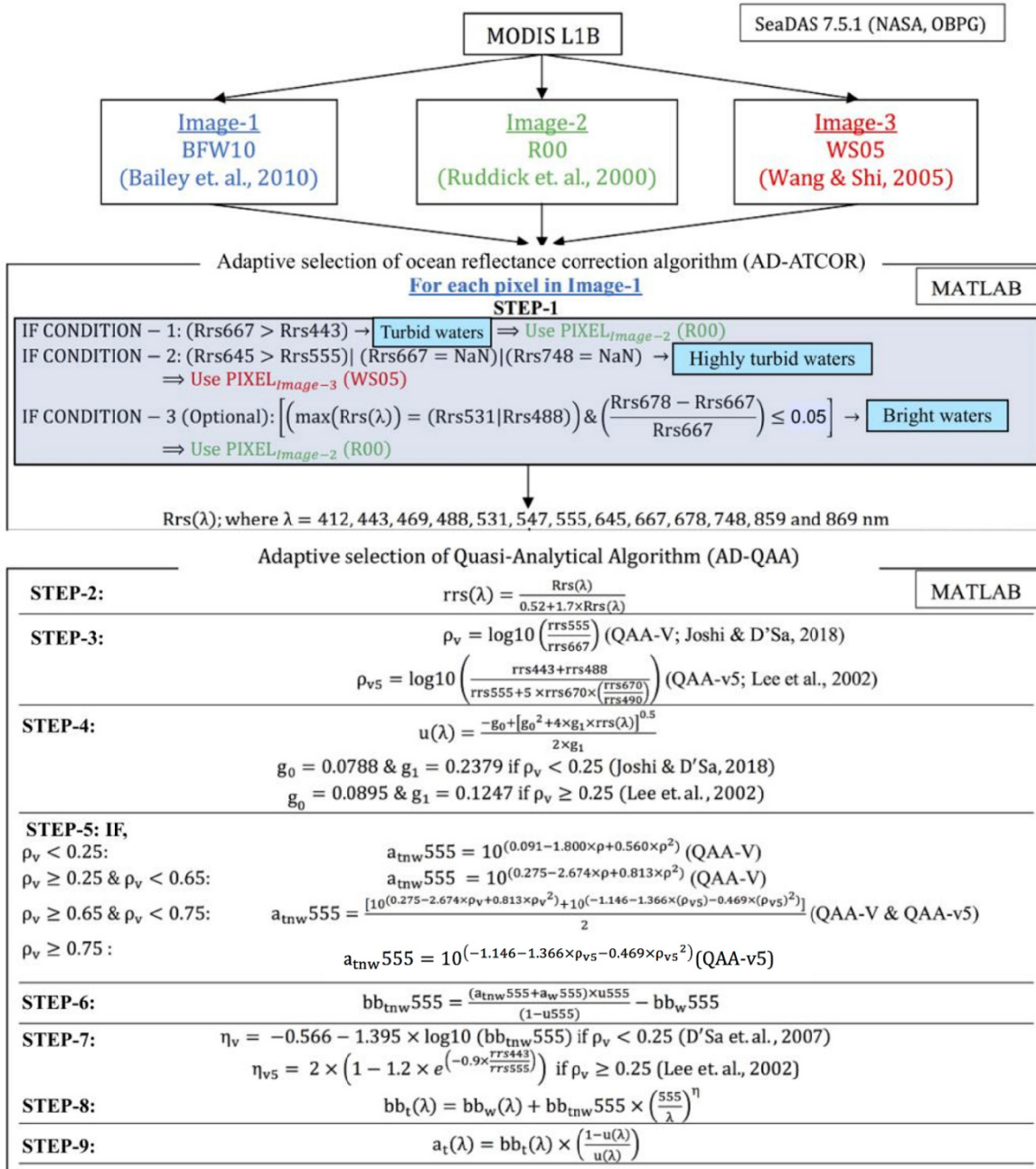## Adaptive selection of NIR/SWIR correction and Quasi analytical algorithms

MODIS L1B

SeaDAS 7.5.1 (NASA, OBPG)

Image-1
BFW10
(Bailey et. al., 2010)

Image-2
R00
(Ruddick et. al., 2000)

Image-3
WS05
(Wang & Shi, 2005)

Adaptive selection of ocean reflectance correction algorithm (AD-ATCOR)

For each pixel in Image-1

MATLAB

STEP-1

IF CONDITION − 1: $(Rrs667 > Rrs443) \rightarrow$ Turbid waters $\Rightarrow$ Use $PIXEL_{Image-2}$ (R00)

IF CONDITION − 2: $(Rrs645 > Rrs555)|(Rrs667 = NaN)|(Rrs748 = NaN) \rightarrow$ Highly turbid waters $\Rightarrow$ Use $PIXEL_{Image-3}$ (WS05)

IF CONDITION − 3 (Optional): $\left[(max(Rrs(\lambda)) = (Rrs531|Rrs488))\,\&\,\left(\frac{Rrs678 - Rrs667}{Rrs667}\right) \leq 0.05\right] \rightarrow$ Bright waters $\Rightarrow$ Use $PIXEL_{Image-2}$ (R00)

$Rrs(\lambda)$; where $\lambda = 412, 443, 469, 488, 531, 547, 555, 645, 667, 678, 748, 859$ and 869 nm

Adaptive selection of Quasi-Analytical Algorithm (AD-QAA)

		MATLAB
STEP-2:	$rrs(\lambda) = \dfrac{Rrs(\lambda)}{0.52 + 1.7 \times Rrs(\lambda)}$	
STEP-3:	$\rho_v = log10\left(\dfrac{rrs555}{rrs667}\right)$ (QAA-V; Joshi & D'Sa, 2018)	
	$\rho_{v5} = log10\left(\dfrac{rrs443 + rrs488}{rrs555 + 5 \times rrs670 \times \left(\frac{rrs670}{rrs490}\right)}\right)$ (QAA-v5; Lee et al., 2002)	

STEP-4:
$$u(\lambda) = \frac{-g_0 + [g_0^2 + 4 \times g_1 \times rrs(\lambda)]^{0.5}}{2 \times g_1}$$
$g_0 = 0.0788 \ \& \ g_1 = 0.2379$ if $\rho_v < 0.25$ (Joshi & D'Sa, 2018)
$g_0 = 0.0895 \ \& \ g_1 = 0.1247$ if $\rho_v \geq 0.25$ (Lee et. al., 2002)

STEP-5: IF,

$\rho_v < 0.25$: $\qquad a_{tnw}555 = 10^{(0.091 - 1.800 \times \rho + 0.560 \times \rho^2)}$ (QAA-V)

$\rho_v \geq 0.25 \ \& \ \rho_v < 0.65$: $\qquad a_{tnw}555 = 10^{(0.275 - 2.674 \times \rho + 0.813 \times \rho^2)}$ (QAA-V)

$\rho_v \geq 0.65 \ \& \ \rho_v < 0.75$: $\qquad a_{tnw}555 = \dfrac{[10^{(0.275 - 2.674 \times \rho_v + 0.813 \times \rho_v^2)} + 10^{(-1.146 - 1.366 \times (\rho_{v5}) - 0.469 \times (\rho_{v5})^2)}]}{2}$ (QAA-V & QAA-v5)

$\rho_v \geq 0.75$: $\qquad a_{tnw}555 = 10^{(-1.146 - 1.366 \times \rho_{v5} - 0.469 \times \rho_{v5}^2)}$ (QAA-v5)

STEP-6: $\qquad bb_{tnw}555 = \dfrac{(a_{tnw}555 + a_w555) \times u555}{(1 - u555)} - bb_w555$

STEP-7: $\qquad \eta_v = -0.566 - 1.395 \times log10\,(bb_{tnw}555)$ if $\rho_v < 0.25$ (D'Sa et. al., 2007)
$\qquad \eta_{v5} = 2 \times \left(1 - 1.2 \times e^{\left(-0.9 \times \frac{rrs443}{rrs555}\right)}\right)$ if $\rho_v \geq 0.25$ (Lee et. al., 2002)

STEP-8: $\qquad bb_t(\lambda) = bb_w(\lambda) + bb_{tnw}555 \times \left(\dfrac{555}{\lambda}\right)^{\eta}$

STEP-9: $\qquad a_t(\lambda) = bb_t(\lambda) \times \left(\dfrac{1 - u(\lambda)}{u(\lambda)}\right)$

Fig. 2. Processing pathway for an adaptive selection of the ocean reflectance correction algorithm (AD-ATCOR) and the QAA (AD-QAA) using the MODIS-Aqua sensor.

hypoxic zone in the nGoM [43]. Examples of the spring and winter phytoplankton blooms, their extent, and the MR plume dispersal on the shelf are shown in Fig. 3. The dominant phytoplankton species and their spatial distribution are mainly controlled by season, river discharge, regional circulation, and wind mixing; however, optical patchiness is often observed due to the coexistence of several phytoplankton species in this dynamic mixing zone where CDOM- and sediment-rich plume water mix with the relatively oligotrophic offshore waters [see Fig. 3(a)–(c)]. Likewise, the optical signature of surface water may rapidly change over a small region that can introduce additional errors in field-satellite

validation analysis. For example, the AERONET-OC site is located in the middle of two river plumes that often result in strong gradients of optically different water types [see Fig. 3(c)].

B. Detecting Different Water Types in an Estuarine to Ocean Continuum Using Spectral Thresholds

Remote sensing reflectance emanating from the surface water carries information about the water itself and its constituents such as dissolved and particulate matter of both organic nature and inorganic nature. Abundance of these constituents plays a vital role in altering the shape of Rrs spectra
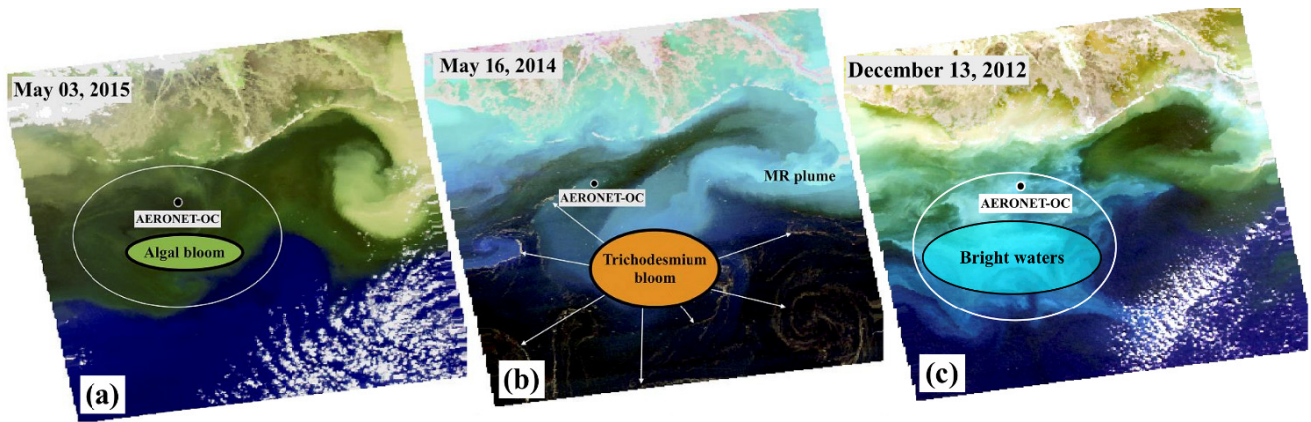
Fig. 3. MODIS-Aqua maps in the nGoM with location of the AERONET-OC site. (a) RGB image shows the extent of an algal bloom over Louisiana shelf during the spring. (b) False color image shows the mixing of sediment-laden MR plume and clear shelf waters. This image also shows *Trichodesmium* blooms (orange strands). (c) RGB image shows the coexistence and extent of phytoplankton species (perhaps green algae and *Coccolithophores*).
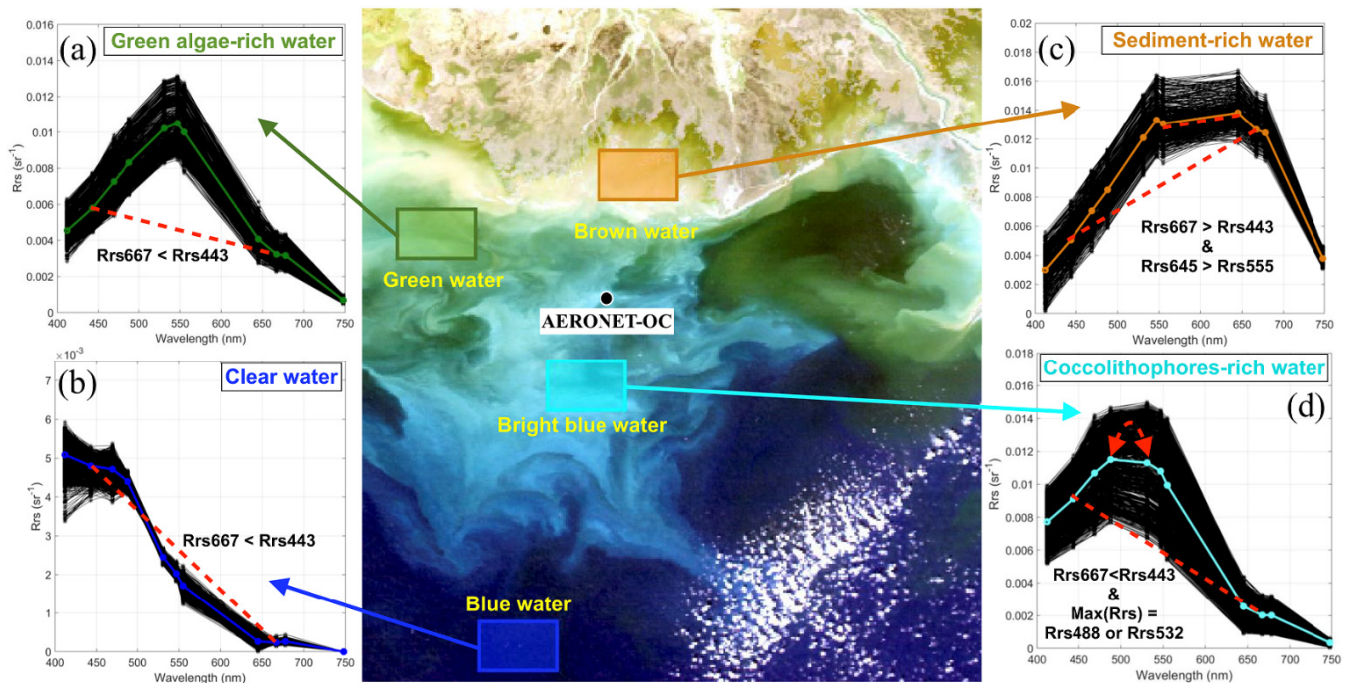

Fig. 4. Different water types in a MODIS-Aqua scene (December 13, 2012) collected over the nGoM. (a) Rrs spectra over the green water. (b) Rrs spectra over the blue water. (c) Rrs spectra over the brown water. (d) Rrs spectra corresponding to the bright blue waters likely due to coccolithophores. Colored lines represent an average of all spectra.

due to their unique absorption, scattering, and fluorescence properties that influence the light field. As shown in Fig. 4, water in a true color satellite scene contains several colors based on relative abundance of a specific water constituent. For example, the green water (green box) represents waters dominated by the green algal cells which give a unique appearance to the Rrs spectra with peaks in the green region (e.g., 531, 547, or 555 nm) [see Fig. 4(a)]. The brown water (orange box) represents mineral-rich water with the Rrs peak shifted toward the red wavelengths [see Fig. 4(b)]. For clear water, the highest Rrs is observed at the blue wavelengths that gradually decrease toward the longer wavelengths due to strong absorption by the water [see Fig. 4(c)]. The occurrence

of *Coccolithophore* bloom-like conditions in the nGOM gives the water a milky or turquoise-white appearance with the Rrs maxima in the blue region contrary to the green region for green algal cells [see Fig. 4(d)] [52]. Additionally, the presence of CDOM may reduce the Rrs signal at the blue and green wavelengths due to strong light absorption in the UV/blue that exponentially decreases toward the green/red wavelengths. Thus, spectrally different water masses (e.g., clear and Chl-a dominated, moderately turbid, and highly turbid) corresponding to dominant water constituents can be separated based on the spectral thresholds for applying water-type-specific atmospheric-correction algorithms in a single satellite scene.

Thus, based on the AD-ATCOR procedure, the three correction algorithms were assigned to different water types, i.e., the BFW10 for clear and Chl-a-dominated waters, the R00 for moderately turbid waters, and the WS05 for highly turbid waters. The first criterion (see Fig. 2 and Section III-C) separates clear and Chl-a-dominated waters from turbid waters using a spectral shape threshold of Rrs667 > Rrs443. For clear water, Rrs443 will always be higher than Rrs667 [see Fig. 4(b)], whereas Chl-a-dominated waters will generally hold this criterion (Rrs667 < Rrs443) as shown in Fig. 4(a) [53]. However, moderate concentrations of mineral particles or CDOM may result in a failure of this criterion (e.g., Rrs667 > Rrs443) in phytoplankton-dominated waters and such water will be considered as turbid water, for which the R00 atmospheric correction algorithm will be used. It is well known that the maximum Rrs peak shifts toward longer wavelengths in surface waters with significant levels of mineral particles [see Fig. 4(c)] [54]; taking into account this information, a second criterion (Rrs645 > Rrs555) is set up to differentiate extremely turbid pixels from turbid water pixels and the WS05 SWIR-correction algorithm is used for such pixels.

Additionally, an optional criterion is set up for bright-water conditions where the Rrs maxima is generally observed at 488 or 531 nm with a very low fluorescence signal at 678 nm. A recent study on optical water-type classification compiled a large data set of SeaWiFS Rrs for *Coccolithophore*-dominated waters and suggested that 96.6% of spectra contains the Rrs maxima at 490 nm [55]. Rrs values of such bright blue water generally fall between clear oceanic water and highly turbid sediment-rich water [see Fig. 4(d)]; hence, they are defined as moderately turbid waters in this study despite their remoteness from the terrestrial influence and the R00 correction algorithm can be optionally applied to these pixels. However, the lack of optical measurements in waters showing coccolithophore-bloom-like conditions necessitates a further evaluation of such assignment in future studies.

C. Validation of Three NIR/SWIR Correction Algorithms at the AERONET-OC Site

Among three correction algorithms, the BFW10 provided the best estimates of Rrs ($R^2 > 0.75$; median ratio = 0.83–1.11; median absolute percentage deviation (MAPD) = 8.1%–26.3%) at all wavelengths [see Fig. 5]. Although the regression lines showed good Rrs estimates at lower values, a noticeable departure of the regression lines from a 1:1 line [see Fig. 5(a)–(e)] and lower slope values (e.g., <1) (see Table I) suggested degrading performance of the BFW10 at the higher Rrs values [see Fig. 5(d) and (e)]. High-Rrs values at 488 and 555 nm indicate the reflective nature of Rrs spectra, perhaps due to the presence of reflective organic and inorganic particles. Even a small time difference between a field measurement and a satellite overpass could contribute to this mismatch as the distribution of SPM rapidly vary in dynamic and productive waters around the AERONET-OC site [56], [57]. The highest was observed at 412 nm (26.3%), whereas the lowest was at 667 nm (8.1%).
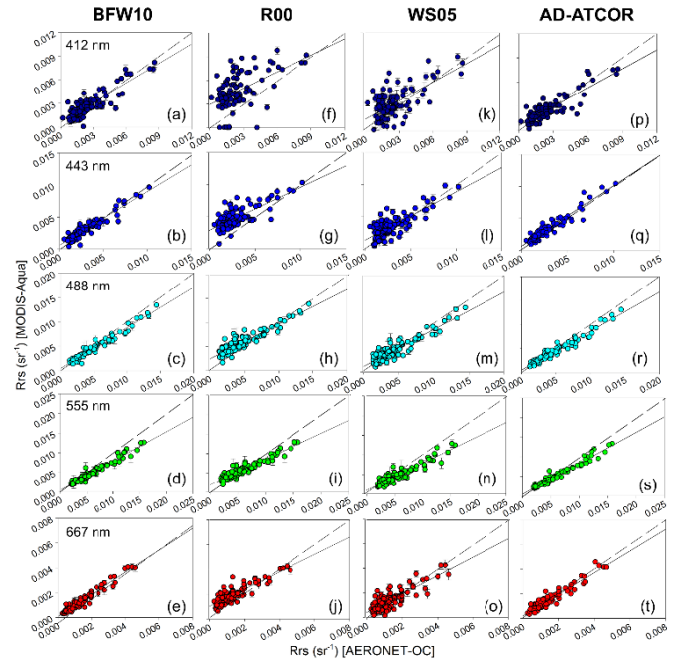

Fig. 5. Validation analysis of the Rrs for three atmospheric correction algorithms. (a)–(e) BFW10, (f)–(j) R00, (k)–(o) WS05, and (p)–(t) AD-ATCOR methodology at five wavelengths (412, 443, 488, 555, and 667 nm) using the MODIS-Aqua imagery and AERONET-OC observations for the nGOM.

A detailed study on the comparison of different NIR-correction algorithms also showed similar trend of high to low MAPD toward longer wavelengths that suggest a large part of these errors is contributed by the bio-optical models used in these algorithms [22].

In contrast, for the R00 algorithm, regression lines showed the lowest slope values (<0.72) and the highest MR (1.27–2.14) among the three algorithms at various wavelengths [see Fig. 5(f)–(j); Table I]. However, the estimates of Rrs improved marginally at the high end, especially at 488, 555, and 667 nm [see Fig. 5(h)–(j)]. Also, the retrieval accuracy was poor at the blue-red wavelengths and significantly improved toward the green wavelength (=15.6%). The validity of core assumptions near the AERONET-OC site could be the primary reason for such a poor performance of the R00. The AERONET-OC site experiences frequent phases of clear to extremely turbid waters due to the interplay of winds, currents, and river discharge. In clear to less turbid water, a backscattering spectrum is largely driven by the pure water scattering, which shows a significant spectral dependence as compared to particle backscattering [24]. Hence, an assumption of invariant ρ_w in the NIR region is not valid in such waters. Similarly, in extremely turbid water, particle backscattering at NIR is significantly higher and thus, $b_{bp}(NIR) \ll a_w(NIR)$ is no longer true and questions the validity of constant water-reflectance ratio assumption [22]. The R00 algorithm is shown to work well for water masses with a specific range of turbidity caused by detritus and mineral matter [23], [24].

The WS05 algorithm showed overall better performance than the R00 with ~50% to 60% decrease in MAPD at

TABLE I

VALIDATION STATISTICS FOR RETRIEVING Rrs USING BFW10, R00, AND WS05 CORRECTION ALGORITHMS AT THE AERONET-OC SITE IN THE nGoM

Correction algorithms	N	Slope	R^2	MR	MAPD (%)
Rrs412					
BFW10	107	**0.82**	0.75	1.11	26.3
R00	107	0.69	0.29	2.14	114.0
WS05	107	0.76	0.46	1.27	43.6
AD-ATCOR	107	0.78	**0.76**	**1.09**	**23.9**
Rrs443					
BFW10	107	0.84	**0.90**	**1.10**	**18.8**
R00	107	0.67	0.57	1.91	90.8
WS05	107	0.76	0.65	1.20	31.4
AD-ATCOR	107	**0.95**	**0.90**	1.11	22.0
Rrs488					
BFW10	107	0.83	**0.96**	**0.96**	9.2
R00	107	0.72	0.85	1.38	34.7
WS05	107	0.77	0.85	1.03	16.1
AD-ATCOR	107	**0.84**	**0.96**	0.95	**9.1**
Rrs555					
BFW10	107	0.75	0.96	0.83	17.6
R00	107	0.66	0.90	1.27	15.6
WS05	107	0.69	0.88	0.87	17.5
AD-ATCOR	107	**0.79**	**0.98**	**0.89**	**14.0**
Rrs667					
BFW10	107	**0.89**	**0.95**	**0.99**	**8.1**
R00	107	0.70	0.74	1.61	59.7
WS05	107	0.75	0.69	1.07	30.8
AD-ATCOR	107	0.88	0.91	1.04	14.9

The number in **bold** represents the best statistical results. **MAPD** = Median absolute percentage deviation that is the median of individual absolute percentage deviation $APD_i = |y_i - x_i|/x_i$, where y_i is a satellite-derived variable and x_i is a field measurement. **MR** =median of individual ratio, y_i/x_i.
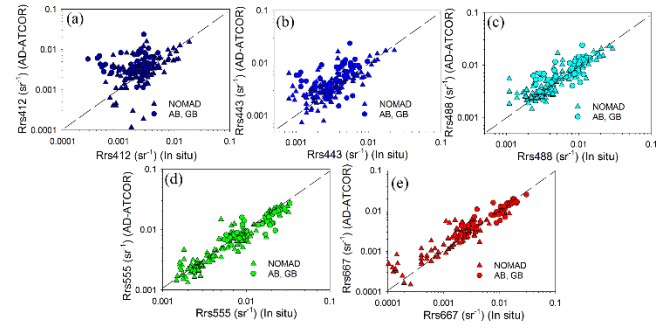

Fig. 6. Validation of the AD-ATCOR-modeled Rrs against field observations of NOMAD (triangles) and the estuarine data set (circles) at (a) 412, (b) 443, (c) 488, (d) 555, and (e) 667 nm.

412 and 667 nm. Also, a notable shift of intercepts toward zero but a marginal change in slope values indicated an improvement in Rrs retrieval in less reflective waters as compared to the R00 [see Fig. 5(k)–(o)]. In principle, the WS05 algorithm is the GW94 atmospheric correction algorithm which uses the black-pixel assumption at the SWIR wavelengths. At the MODIS-Aqua SWIR wavelengths, water absorption is 2–3 orders of magnitude greater than at NIR wavelengths [26]; hence, the assumption of black-pixel is still valid in relatively clearer waters and could be the main reason for its valid performance for several observations at the lower end [see Fig. 5(k)–(o)]. A large scatter could be due to a low SNR of the MODIS-Aqua SWIR bands for ocean color remote sensing [40].

Thus, although each of these ocean reflectance correction algorithms have their merits and demerits in specific water types and individually perform remarkably over a small study area, their application to a larger area or an entire satellite scene is questionable in the presence of different water types.

D. Validation of AD-ATCOR Method

The AD-ATCOR was applied to the MODIS-Aqua imagery to generate a blended Rrs product for its direct evaluation in the nGoM [see Fig. 5(p)–(t)]. The AD-ATCOR showed an obvious improvement as compared to individual correction algorithms at the blue and green wavelengths (see Table I).

Although the BFW10 performed well among the three candidate algorithms and MAPDs were relatively larger for the R00 and the WS05 at blue and red wavelengths (see Table I), the blended satellite product showed a comparable retrieval accuracy for the AERONET-OC data set (=9.1%–23.9%; MR = 0.89–1.11; R^2 = 0.76–0.98) when the three correction algorithms were combined by the AD-ATCOR methodology (see Table I). Furthermore, the AD-ATCOR showed a noteworthy improvement over three standard correction schemes at individual wavelengths (i.e., 412, 488, and 555 nm).

Further assessment of the AD-ATCOR on CDOM- and particle-dominated estuarine data set (Apalachicola Bay and Galveston Bay) showed an acceptable performance at 488, 555, and 667 nm but relatively larger mean APD at 412–443 nm [see Fig. 6(a)—(e)]. The normal distribution of APD is a good measure to ensure the absence of extreme outliers in the validation analysis. Any presence of such outliers would affect the mean statistic and eventually may introduce errors in interpretation of the validation analysis. In such cases of nonnormal distribution, the median can be considered to be the best measure of central tendency. For the estuarine data set, the mean APD is significantly different from the MAPD suggesting a nonnormal distribution of relative errors for the estuarine data set (see Table II). Nevertheless, the MAPDs is smaller than the mean APD suggesting that the AD-ATCOR-retrieved Rrs at all MODIS-Aqua wavelengths with APD less than or equal to the reported median statistics for at least half of the data. This median statistic is similar to the statistic reported for R00 (MUMM) -corrected VIIRS imagery in Galveston Bay, which represents a subset of the estuarine data set of this study [36]. However, larger APDs, especially in the blue, relative to AERONET-OC data could have likely occurred due to the errors introduced by the inherent limitations of individual ocean reflectance correction schemes in shallow and turbid estuarine environments.

When applied to NOMAD, the AD-ATCOR showed relatively poorer performance than the AERONET data set and better performance than the estuarine data set especially at the blue wavelengths (see Tables I and II). In contrast, the poorest validation statistics was observed for NOMAD at the green and red wavelengths among the three data sets (see Table II).

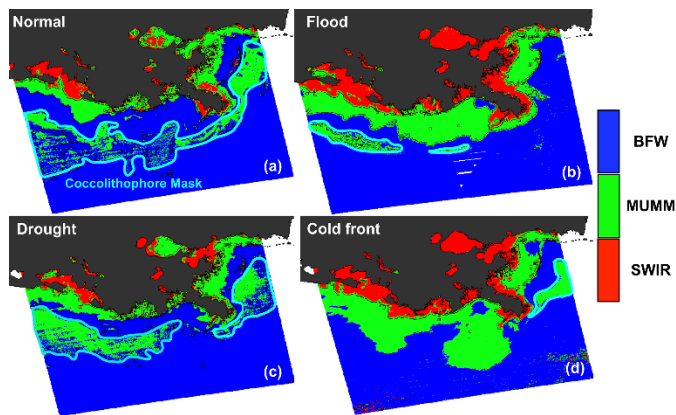| Validation dataset	N	APD (%)			
		Mean	Median (MAPD)	Max.	Min.
Rrs412					
AB, GB	45	294.3	149.2	1937.7	3.5
NOMAD	135	67.5	34.9	804.2	1.4
ALL	**180**	**124.3**	**45.8**	**1937.7**	**1.4**
Rrs443					
AB, GB	45	105.2	61.2	470.7	1.4
NOMAD	135	49.2	23.2	697.9	1.0
ALL	**180**	**63.2**	**27.6**	**697.9**	**1.0**
Rrs488					
AB, GB	45	37.9	22.6	163.7	0.9
NOMAD	135	30.9	17.1	395.3	0.4
ALL	**180**	**32.7**	**17.4**	**395.3**	**0.4**
Rrs555					
AB, GB	45	20.6	16.6	78.7	0.4
NOMAD	134	22.1	16.7	194.4	0.3
ALL	**179**	**21.8**	**16.7**	**194.4**	**0.3**
Rrs667					
AB, GB	45	27.9	12.1	174.4	0.1
NOMAD	94	66.6	28.7	465.5	1.3
ALL	**139**	**54.0**	**22.8**	**465.5**	**0.1**

Fig. 7. Maps showing pixel-by-pixel application of three correction algorithms, BFW10 (blue), R00 (green), and WS05 (red), in heterogeneous waters of nGoM during (a) normal condition (May 6, 2017), (b) MR flood (April 13, 2008), (c) MR drought (October 19, 2012), and (d) passage of a cold front (February 26, 2016). A polygon (cyan color) shows bright water pixels likely due to Coccolithophores (condition-3 in Fig. 2).
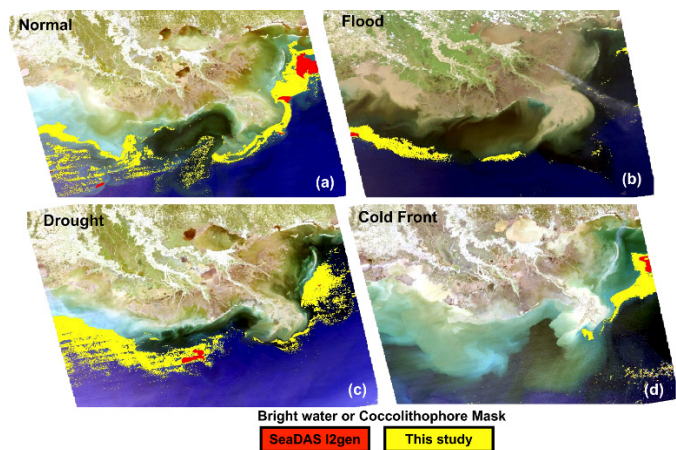

Fig. 8. MODIS-Aqua true color maps showing pixel-by-pixel detection of bright waters in the nGoM during four conditions. (a) Normal condition (May 6, 2017). (b) MR flood (April 13, 2008). (c) MR drought (October 19, 2012). (d) Passage of a cold front (February 26, 2016). SeaDAS l2gen coccolithophore mask (red color) is superimposed on the bright pixel detected by AD-ATCOR approach (yellow color).

Similar to the estuarine data set, the MAPD was much smaller than the mean APD at all wavelengths indicating a better performance of AD-ATCOR on about half of the NOMAD data set with APD $< 35\%$ for various wavelengths. The AD-ATCOR approach does not modify satellite-derived spectra, hence, a significant portion of the observed errors after the application AD-ATCOR approach could have been propagated from the errors in individual ocean reflectance correction approach itself. Therefore, the success of the blending approach is strongly dependent on the success of individual correction algorithm.

To demonstrate a pixel-by-pixel selection of the NIR and SWIR correction algorithms, the AD-ATCOR methodology was applied to the MODIS-Aqua images representing four environmental conditions in the heterogeneous waters of the nGoM (see Fig. 7). These include 1) the normal condition with southeasterly winds (2.5 ms^{-1}) and the MR discharge of $23\,300$ m^{3}s^{-1}; 2) the MR flood condition with river discharge of $35\,950$ m^3 s^{-1} and northwesterly winds (5.4 ms^{-1}); 3) the MR drought condition with river discharge of 4785 m^{3}s^{-1} and northwesterly winds (1.2 ms^{-1}); and 4) a cold front event with northerly winds (4 ms^{-1}) and the MR discharge of $18\,000$ m^{3}s^{-1}. An evaluation area represented a variety of waters ranging from highly turbid Terrebonne Bay and the MR plume waters to the relatively clearer shelf waters. Spectral thresholds of the AD-ATCOR method clearly detected three distinct water types in this heterogeneous environment and applied corresponding correction algorithms (see Fig. 7). For example, the BFW10 algorithm was applied to the relatively clearer open ocean (blue region), whereas the WS05 algorithm was applied in highly turbid water environments (e.g., estuaries, inland turbid lakes, and the vicinity of MR and AR plume waters). In contrast, the R00 algorithm was applied

to moderately turbid waters lying between the highly turbid and clear water types on the Louisiana shelf. Furthermore, the bright water condition (step-1 in Fig. 2) likely detected coccolithophores over a large area that was also much larger than that detected by SeaDAS l2gen coccolithophore mask (see Fig. 8). Using Sentinel-3A OLCI-derived pigment ratios from the bio-optical inversion algorithm, a recent study reported a posthurricane coccolithophore bloom of *Emiliania huxleyi* in northwestern Gulf of Mexico, which also corresponded to the AD-ATCOR's bright water condition in the same region in the MODIS-Aqua image [64].

Fig. 7 also demonstrates the limitation of using a single correction scheme in a dynamic region where seasonality and environmental forcing have a strong influence on the extent of different water types. In such scenarios, the blending approach of AD-ATCOR provides a better solution due to its simplicity and effectiveness in the detection of different

TABLE III
ERROR STATISTICS FOR TWO QAAs AND THE AD-QAA METHOD USING AN ESTUARINE DATA SET

Absolute percentage difference (APD) (%) [Estuarine dataset (Apalachicola Bay and Galveston Bay)]												
	QAA-v5 (Lee et al., 2002)				QAA-V (Joshi & D'Sa, 2018)				AD-QAA (this study)			
λ	N	R^2	Mean	Median (MAPD)	N	R^2	Mean	Median (MAPD)	N	R^2	Mean	Median (MAPD)
Total non-water absorption coefficient (a_{tnw})												
412	45	0.29	53.9	56.8	45	0.38	36.7	36.1	**45**	**0.48**	**33.7**	**35.9**
443	45	0.21	50.7	45.5	45	0.34	34.8	29.5	**45**	**0.43**	**28.4**	**25.2**
488	45	0.51	37.6	38.9	45	0.63	26.9	22.4	**45**	**0.66**	**25.1**	**20.7**
555	45	0.47	35.9	34.3	**45**	**0.69**	**36.1**	**24.3**	45	0.70	36.4	30.3
667	45	0.0	75.3	74.3	45	0.43	75.9	37.8	**45**	**0.48**	84.5	**37.5**
Particulate backscattering coefficient (b_{bp})												
470	20	0.85	43.2	44.0	20	0.76	60.7	26.3	**20**	**0.78**	**43.5**	**41.9**
532	**25**	**0.80**	**35.4**	**32.1**	25	0.71	79.7	60.4	25	0.74	65.1	58.6
660	**12**	**0.88**	**37.7**	**24.2**	12	0.76	171.1	96.5	12	0.80	161.1	97.6

The number in **bold** represents the best statistical results.
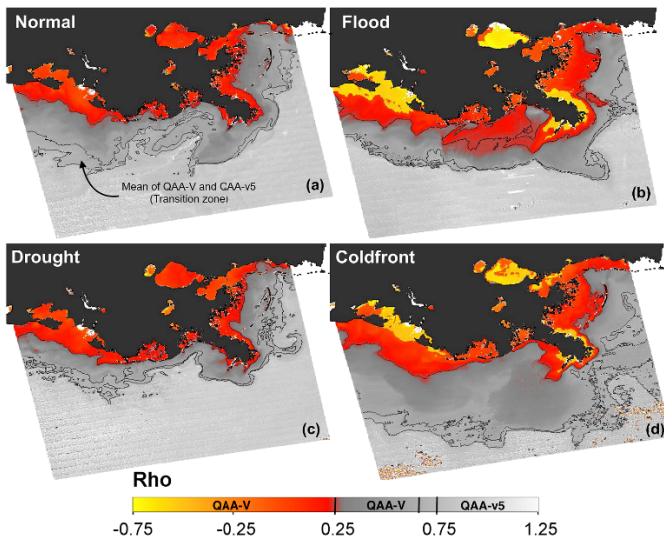
Fig. 9. MODIS-Aqua Rho (ρ) maps showing pixel-by-pixel application (AD-QAA) of two QAAs algorithms, QAA-V and QAA-v5, using ρ thresholds (step-5 in Fig. 2) in heterogeneous waters of nGoM during four conditions. (a) Normal condition (May 6, 2017). (b) MR flood (April 13, 2008). (c) MR drought (October 19, 2012). (d) Passage of a cold front (February 26, 2016).

water types and subsequently in the optimum application of appropriate NIR/SWIR correction algorithm on a pixel-by-pixel basis within a given image.

E. Validation of AD-QAA Method

The AD-ATCOR-derived Rrs spectra were fed into AD-QAA to derive a blended a_{tnw} at the MODIS-Aqua bands and b_{bp} at 470, 532, and 667 nm, respectively. The AD-QAA approach applied the QAA-V or QAA-v5 based on ρ thresholds to different water types (step-5 in Fig. 2). Fig. 9 demonstrates the spatial distribution of ρ for the four environmental conditions in the nGoM. The threshold value of 0.25 separated QAA-V's components (estuarine and nearshore, and shelf waters) and a value of 0.65 restricted its applicability in shelf waters. In contrast, the standard QAA

was applied beyond a ρ value of 0.75 in open ocean, while an average value of both QAAs was used in the transition zone where ρ varied between 0.65 and 0.75. The extent of the transition zone remained small near the river plume but increased away from the river influence. Additionally, seasonality and extreme events also controlled cross-shore movement of various thresholds on the shelf. Therefore, the blending approach of this study appears be a better alternative in a region with heterogeneous water types rather than the use of specific empirical and semi-analytical IOP algorithms.

The standard QAA-v5 showed a negative bias at all wavelengths indicating an overall underestimation of modeled total nonwater absorption and backscattering coefficients [see Fig. 10(a)–10(f)]. A recent study showed similar performance of the standard QAA in estuarine environments and indicated that the use of blue wavelengths and offshore measurements in constructing QAA's empirical relationships could be the primary reason for QAA's degraded performance in turbid waters [36]. For an estuarine data set, the standard QAA (i.e., QAA-v5) showed the poorest performance among three candidates ($R^2 = 0$–0.51; = 34.3–74.3) (see Table III). Rrs spectra from the AD-ATCOR which had large errors at the blue wavelengths (see Table I) could have contributed the most to the errors in the AD-QAA procedure because the primary step of QAA-v5 itself uses the blue bands to estimate the total nonwater absorption coefficient at a reference wavelength (see Fig. 2; Step-5). In contrast, the mean APD values for a_{tnw} were significantly reduced at blue and green wavelengths but increased notably at the red wavelength for NOMAD (see Table IV). A similar trend of high to low APD from blue to red wavelengths was observed for b_{bp}. Despite the coefficients of QAA-v5 being modeled using NOMAD, the QAA-v5 yielded the best estimates of the particulate backscattering coefficient for the estuarine data set (see Table III).

The QAA-V showed an overall positive mean bias (MB) at all wavelengths excluding 412 nm, suggesting an overall overestimation of modeled absorption and backscattering coefficients [see Fig. 10(g)–(l)]. However, the mean APD values for a_{tnw} were reduced by about 17% at 412 nm, 16% at
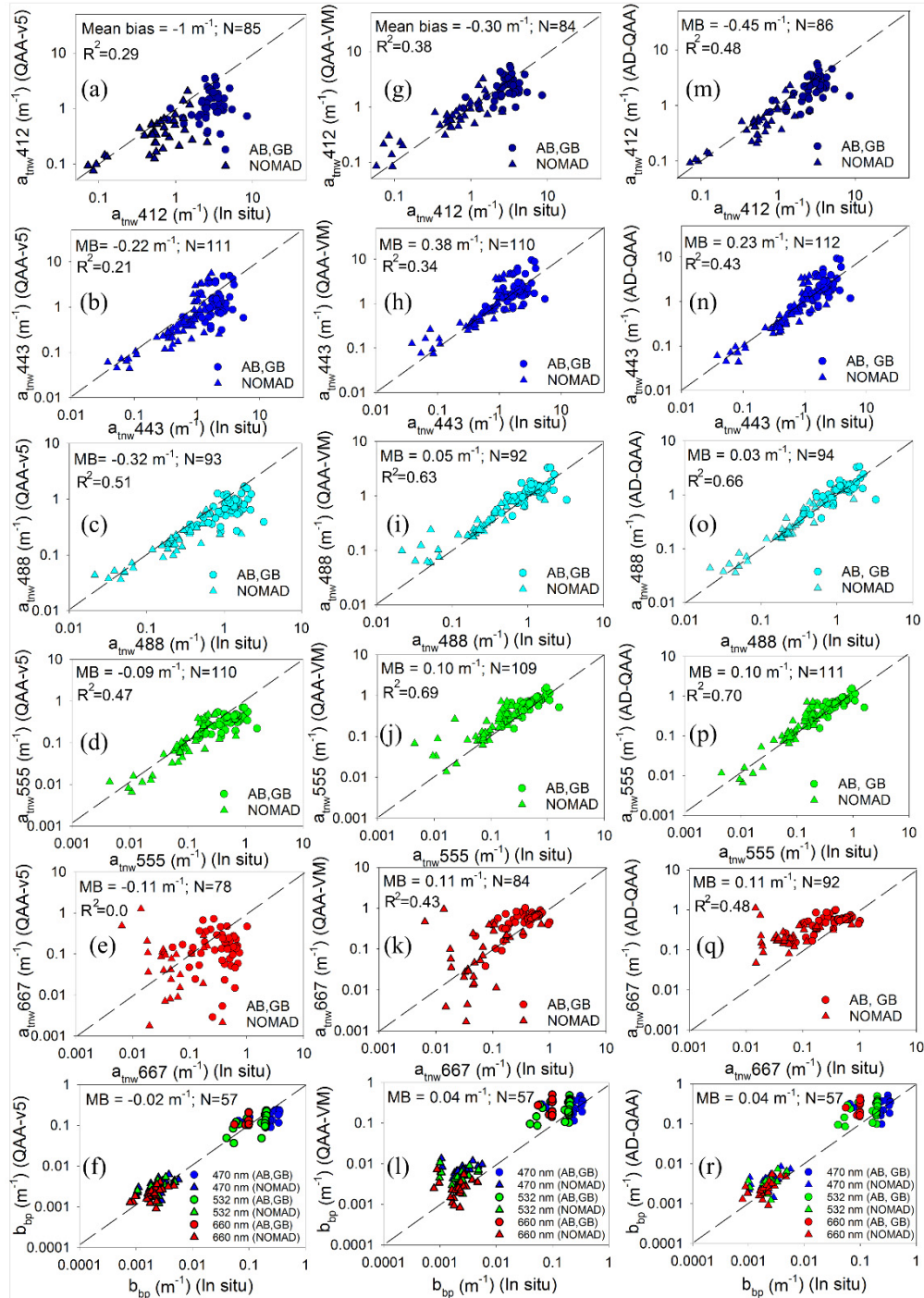
Fig. 10. Validation of (a)–(f) QAA-v5, (g)–(l) QAA-V (or QAA-VM for MODIS Aqua), and (m)–(r) AD-QAA-derived IOPs (total nonwater absorption and backscattering coefficients) against field observations of NOMAD (triangles) and the estuarine (circles) data sets.

443 nm, and 11% at 488 nm, whereas a notable increase in the mean APD was observed for b_{bp} at the three wavelengths when QAA-V and QAA-v5 were compared using the estuarine data set (see Table III). Joshi and D'Sa [36] showed similar results for estuarine observations; however, the errors were relatively smaller at 443 nm since *in situ* Rrs spectra were used in QAA-V rather than satellite Rrs products in their validation analysis [see Fig. 6(b)]. The empirical relationships in the QAA-V was tuned using field data obtained in various estuaries [36]; hence, despite the mean APD values indicating a weaker performance of QAA-V on NOMAD at all wavelengths, a large departure of MAPD and relatively lower values than the mean APD indicated that the QAA-V does perform reasonably well for a subset of NOMAD that is representing estuarine and near-shore waters (see Table IV). The MAPDs at the blue wavelengths were similar to the error statistics reported in Joshi and D'Sa [36] for NOMAD [see Fig. 7(c)].

TABLE IV

ERROR STATISTICS FOR TWO QAAs AND THE AD-QAA METHOD USING NOMAD

Absolute percentage difference (APD) (%) [NOMAD]												
QAA-v5 (Lee et al., 2002)					QAA-V (Joshi & D'Sa, 2018)				AD-QAA (this study)			
λ	N	R^2	Mean	Median	N	Mean	R^2	Median	N	R^2	Mean	Median
Total non-water absorption coefficient (a_{tnw})												
412	40	0.59	38.6	33.9	39	51.9	0.74	32.7	**41**	**0.80**	**29.9**	**26.3**
443	58	0.67	35.9	31.9	57	50.7	0.73	18.8	**59**	**0.81**	**25.9**	**25.6**
488	40	0.79	27.8	22.6	59	49.5	0.81	21.9	**41**	**0.90**	**23.2**	**15.8**
555	**57**	**0.80**	**38.3**	**28.6**	56	125.4	0.66	56.1	58	0.88	67.6	40.9
667	28	0.11	729.7	87.1	31	543.2	0.11	**70.3**	39	0.10	340.2	108.1
Particulate backscattering coefficient (b_{bp})												
470	**24**	**0.26**	**54.5**	**48.2**	24	221.4	0.0	163.1	24	0.34	77.2	55.8
532	**24**	**0.30**	**42.1**	**33.9**	24	148.5	0.0	98.3	24	0.29	51.2	49.2
660	**24**	**0.37**	**27.9**	**28.9**	24	72.8	0.0	21.9	24	0.26	39.4	30.4

The number in **bold** represents the best statistical results.

The blended QAA (AD-QAA) performed overall better in estimating the total absorption coefficient than the QAA-v5 and the QAA-V [see Fig. 10(m)–(r)] for both NOMAD and the estuarine data set. Although the MB and R^2 improved at various wavelengths, the errors, however, increased toward longer wavelengths (see Tables III and IV) for the estuarine data set and NOMAD. For the particle backscattering, the AD-QAA methodology did not show a notable improvement (see Fig. 10(r); Table IV) over the QAA-v5 likely due to the poor performance of QAA-V in estimating b_{bp}; however, the error statistics show intermediate values between the QAA-v5 and QAA-V suggesting an overall improvement by the blending approach.

F. Performance Evaluation of the AD-QAA Approach Under Contrasting Environmental Conditions in the nGoM

For the direct comparison of QAA-v5, QAA-V, and AD-QAA, the proposed methodology was applied to the MODIS-Aqua images representing four conditions in the most dynamic region of the nGoM. An evaluation transect represents a variety of waters ranging from highly turbid Terrebonne Bay and the MR plume waters to the relatively clearer shelf waters (see Fig. 11).

The three QAAs showed similar variations in the total nonwater absorption coefficient (a_{tnw}443) along the transect; however, their magnitude clearly varied at different locations under different conditions. During the normal condition, Terrebonne Bay [pixel no. 0–25 in Fig. 11(a)] showed the highest a_{tnw}443 followed by the MR plume [225–300 in Fig. 11(a)] and shelf waters [50–200 in Fig. 11(a)]. The Ship Shoal, an important region for sand mining [58] located to the south of Terrebonne Bay, also experienced elevated a_{tnw}443 ($\sim$0.5 to 0.75 m^{-1}), likely due to CDOM and particulate absorption [59]. The QAA-v5, however, showed relatively lower a_{tnw}443 in the estuary and the MR plume, while the QAA-V exhibited higher a_{tnw}443 at these locations. It has been previously shown that the QAA-V performs better than QAA-v5 in turbid estuarine and nearshore waters, whereas QAA-v5 is superior over QAA-V

in relatively clearer waters [36]. The AD-QAA procedure, in contrast, provided similar results as QAA-V in turbid waters and as QAA-v5 in clear waters, whereas intermediate values in the transition zone (e.g., to the South of the MR plume; 300–350 in Fig. 11(a).

During the MR flood, the Louisiana shelf experienced high values of a_{tnw}443 likely due to the elevated terrestrial inputs linked to high freshwater discharge [see Fig. 11(b)] [60], [61]. As compared to the normal condition, the width of the plume was small but its amplitude was almost double indicating a strong intrusion of freshwater plume into the offshore waters [red lines, Fig. 11(b)]. The Ship Shoal region showed a distinct peak likely due to sediment resuspension under strong flow and wind conditions [59]. Although the shape of a_{tnw}443 change is retained by the three algorithms along the entire transect, the standard QAA-v5 yielded significantly lower a_{tnw}443 during the MR flood condition [Fig. 11(b)]. The AD-QAA-derived a_{tnw}443 were, however, similar to QAA-V over the turbid shelf waters ($\sim$1 m^{-1}) and showed values between the results of two QAAs (QAA-V and QAA-v5) in the transition zone [275–350 in Fig. 11(b)].

The lowest a_{tnw}443 were observed over the entire shelf region during the MR drought. The MR plume was absent from the transect [see Fig. 11(c)]. Although AD-QAA showed a_{tnw}443 values similar to QAA-V in Terrebonne Bay, it matched QAA-v5 over the entire shelf under the low flow conditions [inset; Fig. 11(c)]. In contrast, the cold front condition showed the highest values of a_{tnw}443 along the entire transect with elevated values extending over the entire shelf. The a_{tnw}443 values to the south of the MR plume were about two times higher than during the strong flood condition. Rrs spectra corresponding to this region were similar to Class 4 waters as classified in Vantrepotte *et al.* [62] suggesting the dominance of phytoplankton and CDOM near the MR delta. Interestingly, all algorithms showed similar performance in phytoplankton- and CDOM-dominated region [yellow box, Fig. 11(d)], but QAA-V and QAA-AD showed relatively higher estimates of absorption coefficients in Terrebonne Bay and Ship Shoal region likely due to high amounts of CDOM and mineral
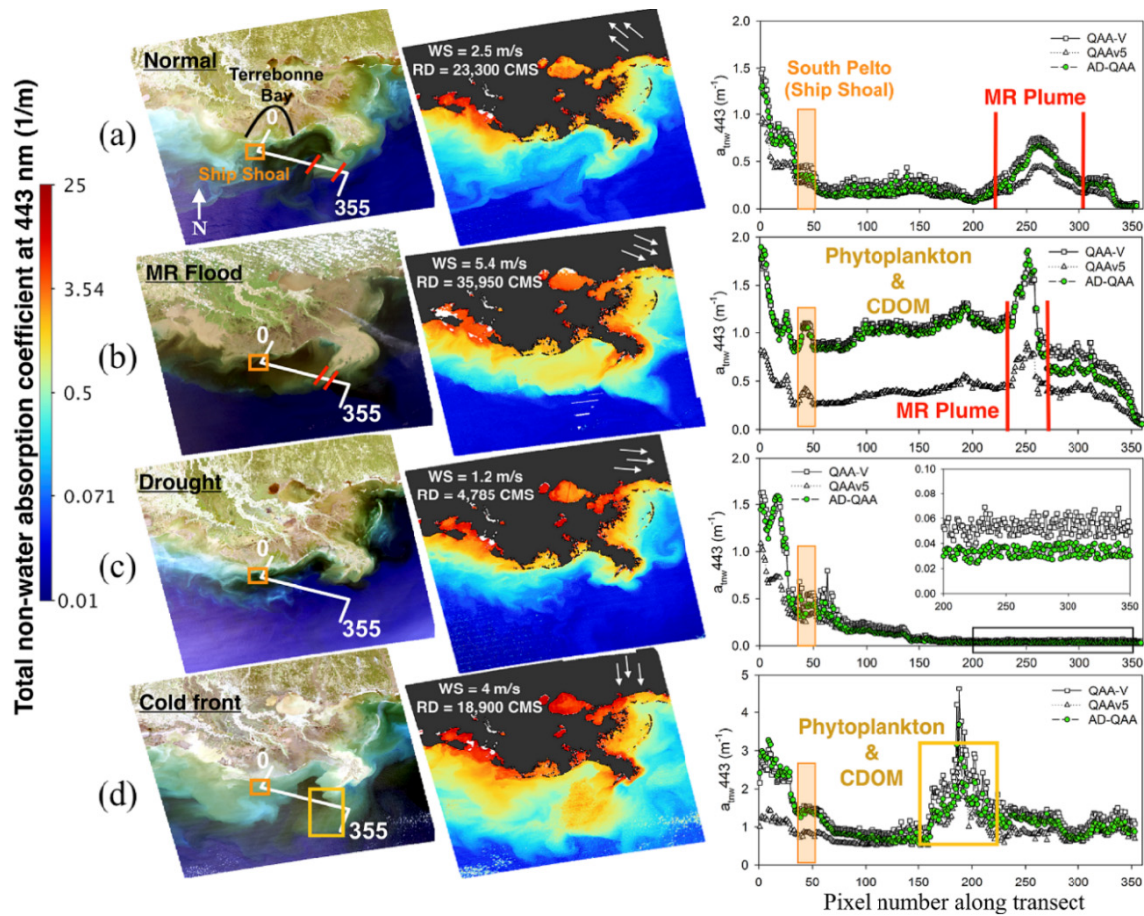
Fig. 11. MODIS-Aqua maps for AD-ATCOR and AD-QAA-derived total nonwater absorption coefficients during (a) normal condition (May 6, 2017), (b) MR flood (April 13, 2008), (c) MR drought (October 19, 2012), and (d) passage of a cold front (February 26, 2016). RGB image and $a_{tnw}443$ maps corresponding to these events are shown in the first and the second columns, whereas the $a_{tnw}443$ variability along the transect (white line) is shown in the third column, where x-axis represents pixel number along transect. Two red lines represent an approximate width of the MR plume along the transect. The orange box represents a location of the ship shoal. A yellow box shows phytoplankton and CDOM-dominated waters near the plume. WS is wind speed in ms^{-1} and RD is river discharge in cubic meters per second (m^3s^{-1}).

particles (Class 3 [59]) caused by sediment resuspension under strong wind condition [orange box, Fig. 11(d)] [59].

Particulate backscattering coefficients ($b_{bp}555$) varied similar to $a_{tnw}443$ under different conditions, showing analogous trends for the three QAAs along the transect (see Fig. 12). The AD-QAA showed the trend and magnitudes of $b_{bp}555$ similar to QAA-V in turbid regions (e.g., Terrebonne Bay and the MR plume), whereas they shifted toward QAA-v5 in the relatively clearer waters. The backscattering coefficients in Terrebonne Bay and shelf waters were similar to previously reported values in a neighboring estuary—Barataria Bay [36] and the MR plume region [63]. Contrary to the absorption coefficient, the map of particulate backscattering coefficient additionally suggested the presence of bright waters likely due to *Coccolithophores* during the normal condition [see Figs. 7(a) and 12(a)] and the MR plume during the frontal passage [see Fig. 12(d)]. However, little is known about IOPs associated with these events, especially related to those obtained from the QAAs. Overall, the AD-QAA approach tends to seamlessly switch between and blend the QAA-V and QAA-v5 along the transects with contrasting water types.

G. Sources of Errors and Limitations of the AD-ATCOR and AD-QAA Methods

The adaptive selection of the atmospheric-correction algorithm and QAA may suffer from large errors propagated from the source products, intermediate steps, and underlying assumptions in the AD-ATCOR and the AD-QAA models that could have contributed to the significant errors in validation statistics in this study. The overall errors that are reported in the blended IOP products may include but are not limited to the following sources of errors.

1) The candidate atmospheric correction algorithms (i.e., BFW10, R00, and WS05) have limited application in a specific water type or in a small region due to their core assumptions and/or bio-optical empirical models. When applied to optically dynamic environments, such assumptions and empirical models are often known to show unsatisfactory performance and to cause large errors which perhaps propagate to the AD-ATCOR procedure and subsequently, to the AD-QAA.

2) The spectral thresholds in AD-ATCOR (step-1; Fig. 2) can also cause errors in generating a blended satellite
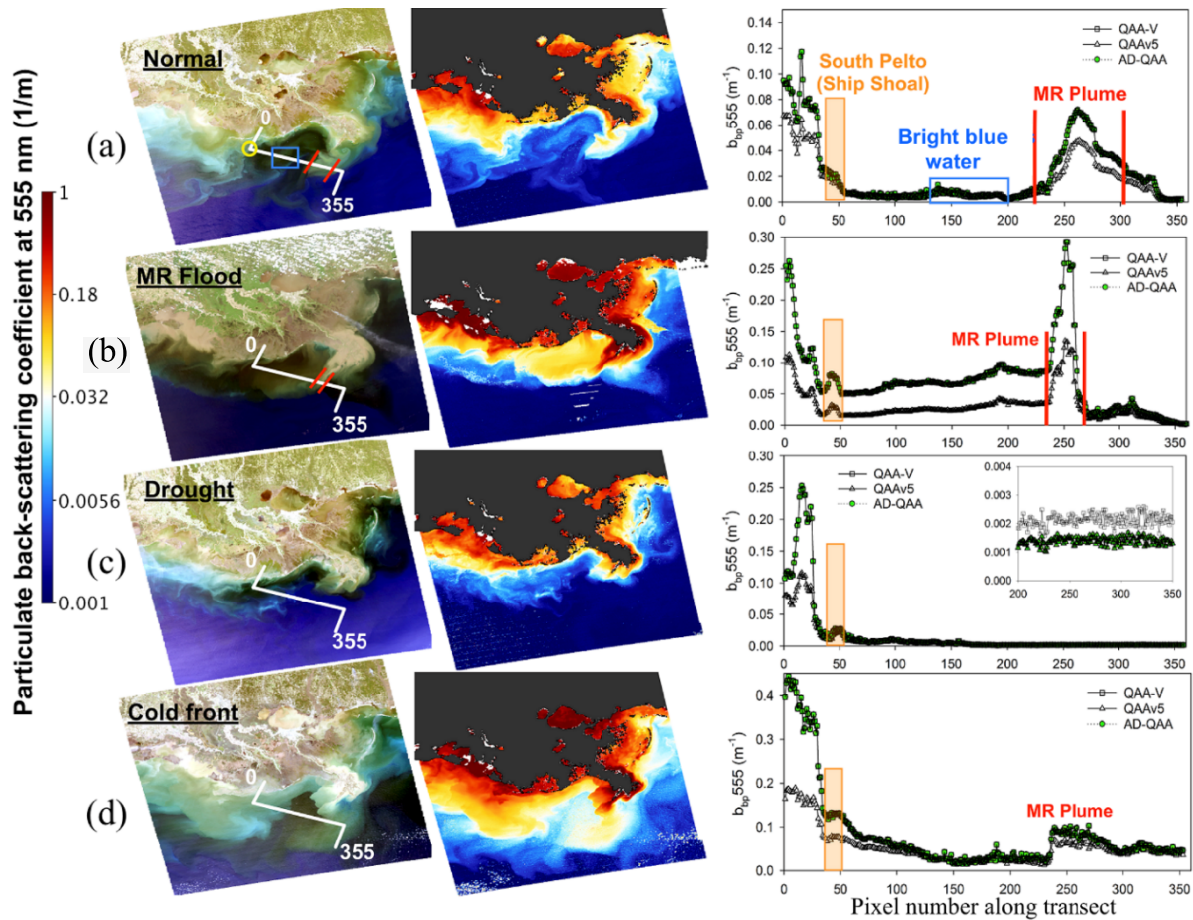
Fig. 12. MODIS-Aqua maps for AD-ATCOR and AD-QAA-derived total nonwater scattering coefficients during (a) normal condition (May 6, 2017), (b) MR flood (April 13, 2008), (c) MR drought (October 19, 2012), and (d) passage of a cold front (February 26, 2016). RGB image and $b_{bp}443$ maps corresponding to these events are shown in the first and the second columns, whereas the variation of $a_{bp}443$ along the transect (while line) is shown in the third column where x-axis represents pixel number along transect. Two red lines represent an approximate width of the MR plume along transect. The yellow circle represents a location of the ship shoal.

product because the natural system cannot be explained completely by such simple thresholds. As a result, a smooth transition from one water type to another is difficult to achieve and a blended satellite imagery may show noticeable difference at the boundary between two water masses, especially when a sharp gradient in water color is observed in a study region.

3) Beside the errors in the QAA procedure, the threshold-based blending of QAAs (step-5; Fig. 2) could perhaps cause additional errors, especially in the transition zone, because the structure of the core empirical models (QAA-v5 and QAA-V) is quite different and using an average of both algorithms in the transition zone may be a better but not an accurate solution.

4) The uncertainties in the field measurements in the AERONET-OC, NOMAD, and estuarine data sets could also be a potential source of error in the validation statistics of this study. Some examples of such sources include but not limited to the measurement errors in above-water nL_w from AERONET-OC, the propagation

of in-water Rrs to just above the surface at several NOMAD stations, the selection of appropriate surface reflectance factor and sun-glint correction necessary for obtaining Rrs from above-water radiance measurements, and the methodological differences in field and laboratory IOP measurements, including differences in instrumentation and measurement protocols among various groups in NOMAD.

V. CONCLUSION

We proposed a methodology for AD-ATCOR and AD-QAA algorithms for the MODIS-Aqua sensor to utilize the strengths of different NIR/SWIR correction algorithms and QAA algorithms within a satellite scene with contrasting water types, ranging from turbid coastal to the clear open ocean waters. A comparison of three NIR/SWIR reflectance correction algorithms (i.e., BFW10, R00, and WS05) showed that the iterative NIR algorithm often outperformed the other two in less turbid water, whereas R00 and WS05 performed reasonably well in relatively turbid waters. A blended Rrs product from AD-ATCOR procedure was compared with the *in*

situ measurements from AERONET-OC station in the nGoM. The validation analysis from this effort showed overall good agreement of the AD-ATCOR-derived Rrs and AERONET-OC-measured Rrs at various wavelengths. Additional assessment of the AD-ATCOR on NOMAD and the estuarine data set suggested that the application of AD-ATCOR or similar procedure appears to be a better alternative to overcome limitations of the traditional NIR/SWIR reflectance correction algorithms especially in the estuarine-coastal-oceanic transition regions.

The blended MODIS-Aqua Rrs product from the AD-ATCOR procedure was then used as an input to the AD-QAA procedure. The AD-QAA procedure merges two QAA (QAA-v5 and QAA-V) based on a threshold of green to red band ratio as suggested in Joshi and D'Sa [36] to provide blended IOPs (i.e., total nonwater absorption and particle backscattering coefficients) product. The AD-QAA-derived IOPs were then validated against field observations from Apalachicola Bay, Galveston Bay, and NOMAD. AD-QAA showed the lowest errors in retrieving a_{tnw} and b_{bp} at the MODIS blue bands as compared to the two QAAs, with some gradual performance degradation toward the green and red wavelengths, especially for NOMAD.

The combined sequential application of the AD-ATCOR and AD-QAA procedures to the MODIS-Aqua imagery representing four environmental conditions in the nGoM demonstrated modest to significant improvements over the nonadaptive schemes in highly contrasting water types where surface water properties are influenced by the combined forcing of two large rivers, winds, and strong currents. Since the accurate retrieval of IOPs and in-water constituents from ocean color remote sensing is a persistent problem in many important coastal zones, the strengths of the AD-ATCOR and AD-QAA procedures can be explored further in other optically complex regions and further extended to other current and future ocean color sensors with spectral resolution equivalent to or better than the MODIS-Aqua sensor.

ACKNOWLEDGMENT

REFERENCES

[1] P. G. Falkowski, "The role of phytoplankton photosynthesis in global biogeochemical cycles," *Photosynth. Res.*, vol. 39, no. 3, pp. 235–258, Mar. 1994, doi: 10.1007/BF00014586.

[2] D. Stramski and S. B. Woźniak, "On the role of colloidal particles in light scattering in the ocean," *Limnol. Oceanogr.*, vol. 50, no. 5, pp. 1581–1591, Sep. 2005, doi: 10.4319/lo.2005.50.5.1581.

[3] P. G. Coble, "Marine optical biogeochemistry: The chemistry of ocean color," *Chem. Rev.*, vol. 107, no. 2, pp. 402–418, 2007, doi: 10.1021/cr050350.

[4] V. J. Hill, "Impacts of chromophoric dissolved organic material on surface ocean heating in the Chukchi sea," *J. Geophys. Res., Oceans*, vol. 113, no. C7, 2008, doi: 10.1029/2007JC004119.

[5] M. F. Fitzsimons, M. C. Lohan, A. D. Tappin, and G. E. Millward, "The role of suspended particles in estuarine and coastal biogeochemistry," in *Treatise on Estuarine and Coastal Science*, E. Wolanski and D. McLusky, Eds. Waltham, MA, USA: Academic, 2011, pp. 71–114.

[6] C. S. Roesler and E. Boss, *In Situ Measurement of the Inherent Optical Properties (IOPs) and Potential for Harmful Algal Bloom Detection and Coastal Ecosystem Observations*. Paris, France: UNESCO, 2008, pp. 153–206.

[7] E. Boss *et al.*, "Comparison of inherent optical properties as a surrogate for particulate matter concentration in coastal waters," *Limnol. Oceanogr. Methods*, vol. 7, no. 11, pp. 803–810, Nov. 2009, doi: 10.4319/lom.2009.7.803.

[8] C. S. Roesler and A. H. Barnard, "Optical proxy for phytoplankton biomass in the absence of photophysiology: Rethinking the absorption line height," *Methods Oceanogr.*, vol. 7, pp. 79–94, Sep. 2013, doi: 10.1016/j.mio.2013.12.003.

[9] I. D. Joshi *et al.*, "Assessing chromophoric dissolved organic matter (CDOM) distribution, stocks, and fluxes in Apalachicola Bay using combined field, VIIRS ocean color, and model observations," *Remote Sens. Environ.*, vol. 191, pp. 359–372, Mar. 2017, doi: 10.1016/j.rse.2017.01.039.

[10] C. R. McClain, "A decade of satellite ocean color observations," *Annu. Rev. Mar. Sci.*, vol. 1, no. 1, pp. 19–42, Jan. 2009, doi: 10.1146/annurev.marine.010908.163650.

[11] M. Wang *et al.*, "VIIRS ocean color research and applications," in *Proc. IEEE Int. Geosci. Remote Sens. Symp. (IGARSS)*, Jul. 2015, pp. 2911–2914, doi: 10.1109/IGARSS.2015.7326424.

[12] H. R. Gordon and D. K. Clark, "Clear water radiances for atmospheric correction of coastal zone color scanner imagery," *Appl. Opt.*, vol. 20, no. 24, p. 4175, Dec. 1981, doi: 10.1364/AO.20.004175.

[13] A. Morel and B. Gentili, "Diffuse reflectance of oceanic waters III Implication of bidirectionality for the remote-sensing problem," *Appl. Opt.*, vol. 35, no. 24, p. 4850, Aug. 1996, doi: 10.1364/AO.35.004850.

[14] H. R. Gordon and M. Wang, "Retrieval of water-leaving radiance and aerosol optical thickness over the oceans with SeaWiFS: A preliminary algorithm," *Appl. Opt.*, vol. 33, no. 3, p. 443, Jan. 1994, doi: 10.1364/AO.33.000443.

[15] C. Hu, K. L. Carder, and F. E. Muller-Karger, "Atmospheric correction of SeaWiFS imagery over turbid coastal waters," *Remote Sens. Environ.*, vol. 74, no. 2, pp. 195–206, Nov. 2000, doi: 10.1016/s0034-4257(00)00080-8.

[16] K. G. Ruddick, F. Ovidio, and M. Rijkeboer, "Atmospheric correction of SeaWiFS imagery for turbid coastal and inland waters," *Appl. Opt.*, vol. 39, no. 6, p. 897, Feb. 2000, doi: 10.1364/AO.39.000897.

[17] R. Stumpf, R. Arnone, R. Gould, P. Martinolich, and V. Ransibrahmanakul, "A partially coupled ocean-atmosphere model for retrieval of water-leaving radiance from SeaWiFS in coastal waters," NASA, Washington, DC, USA, Tech. Rep. 206892, 2003, pp. 51–59.

[18] M. Wang and W. Shi, "Estimation of ocean contribution at the MODIS near-infrared wavelengths along the east coast of the U.S.: Two case studies," *Geophys. Res. Lett.*, vol. 32, 2005, Art. no. L13606, doi: 10.1029/2005GL022917.

[19] M. Wang and W. Shi, "The NIR-SWIR combined atmospheric correction approach for MODIS ocean color data processing," *Opt. Express*, vol. 15, no. 24, p. 15722, 2007, doi: 10.1364/OE.15.015722.

[20] S. W. Bailey, B. A. Franz, and P. J. Werdell, "Estimation of near-infrared water-leaving reflectance for satellite ocean color data processing," *Opt. Express*, vol. 18, no. 7, p. 7521, Mar. 2010, doi: 10.1364/OE.18.007521.

[21] X. He, Y. Bai, D. Pan, J. Tang, and D. Wang, "Atmospheric correction of satellite ocean color imagery using the ultraviolet wavelength for highly turbid waters," *Opt. Express*, vol. 20, no. 18, Aug. 2012, Art. no. 20754, doi: 10.1364/OE.20.020754.

[22] C. Jamet, H. Loisel, C. P. Kuchinke, K. Ruddick, G. Zibordi, and H. Feng, "Comparison of three SeaWiFS atmospheric correction algorithms for turbid waters using AERONET-OC measurements," *Remote Sens. Environ.*, vol. 115, no. 8, pp. 1955–1965, Aug. 2011, doi: 10.1016/j.rse.2011.03.018.

[23] C. Goyens, C. Jamet, and T. Schroeder, "Evaluation of four atmospheric correction algorithms for MODIS-Aqua images over contrasted coastal waters," *Remote Sens. Environ.*, vol. 131, pp. 63–75, Apr. 2013, doi: 10.1016/j.rse.2012.12.006.

[24] K. G. Ruddick, V. De Cauwer, Y.-J. Park, and G. Moore, "Seaborne measurements of near infrared water-leaving reflectance: The similarity spectrum for turbid waters," *Limnol. Oceanogr.*, vol. 51, no. 2, pp. 1167–1179, Mar. 2006, doi: 10.4319/lo.2006.51.2.1167.

[25] M. Wang, J. Tang, and W. Shi, "MODIS-derived ocean color products along the China east coastal region," *Geophys. Res. Lett.*, vol. 34, 2007, Art. no. L06611, doi: 10.1029/2006GL028599.

[26] M. Wang, S. Son, and W. Shi, "Evaluation of MODIS SWIR and NIR-SWIR atmospheric correction algorithms using SeaBASS data," *Remote Sens. Environ.*, vol. 113, no. 3, pp. 635–644, Mar. 2009, doi: 10.1016/j.rse.2008.11.005.

[27] D. Aurin, A. Mannino, and B. Franz, "Spatially resolving ocean color and sediment dispersion in river plumes, coastal systems, and continental shelf waters," *Remote Sens. Environ.*, vol. 137, pp. 212–225, Oct. 2013, doi: 10.1016/j.rse.2013.06.018.

[28] Z. Lee, K. L. Carder, and R. A. Arnone, "Deriving inherent optical properties from water color: A multiband quasi-analytical algorithm for optically deep waters," *Appl. Opt.*, vol. 41, no. 27, p. 5755, Sep. 2002.

[29] Z. Lee, B. Lubac, J. Werdell, and R. Arnone, "An update of the quasi-analytical algorithm (QAA_v5)," Int. Ocean Colour Coordinating Group, Tech. Rep., 2009. Accessed: Feb. 16, 2020. [Online]. Available: http://www.ioccg.org/groups/software.html

[30] Z. Lee, R. Arnone, C. Hu, P. J. Werdell, and B. Lubac, "Uncertainties of optical parameters and their propagations in an analytical ocean color inversion algorithm," *Appl. Opt.*, vol. 49, no. 3, p. 369, Jan. 2010, doi: 10.1364/AO.49.000369.

[31] S. Qing, J. Tang, T. Cui, and J. Zhang, "Retrieval of inherent optical properties of the yellow sea and east China sea using a quasi-analytical algorithm," *Chin. J. Ocean. Limnol.*, vol. 29, no. 1, pp. 33–45, Jan. 2011.

[32] W. Zhu, Q. Yu, Y. Q. Tian, R. F. Chen, and G. B. Gardner, "Estimation of chromophoric dissolved organic matter in the Mississippi and Atchafalaya river plume regions using above-surface hyperspectral remote sensing," *J. Geophys. Res.*, vol. 116, no. C2, pp. 1–22, Feb. 2011.

[33] S. Mishra, D. R. Mishra, Z. Lee, and C. S. Tucker, "Quantifying cyanobacterial phycocyanin concentration in turbid productive waters: A quasi-analytical approach," *Remote Sens. Environ.*, vol. 133, pp. 141–151, Jun. 2013.

[34] C. Mitchell, A. Cunningham, and D. McKee, "Remote sensing of particulate absorption coefficients and their biogeochemical interpretation: A case study in the Irish sea," *Remote Sens. Environ.*, vol. 152, pp. 74–82, Sep. 2014.

[35] G. Zheng, D. Stramski, and R. A. Reynolds, "Evaluation of the quasi-analytical algorithm for estimating the inherent optical properties of seawater from ocean color: Comparison of Arctic and lower-latitude waters," *Remote Sens. Environ.*, vol. 155, pp. 194–209, Dec. 2014, doi: 10.1016/j.rse.2014.08.020.

[36] I. D. Joshi and E. J. D'Sa, "An estuarine-tuned quasi-analytical algorithm (QAA-V): Assessment and application to satellite estimates of SPM in Galveston Bay following Hurricane Harvey," *Biogeosciences*, vol. 15, no. 13, pp. 4065–4086, Jul. 2018, doi: 10.5194/bg-15-4065-2018.

[37] H. R. Gordon, "Atmospheric correction of ocean color imagery in the Earth Observing System era," *J. Geophys. Res.*, vol. 102, no. D14, pp. 17081–17106, Jul. 1997, doi: 10.1029/96JD02443.

[38] L. Jiang and M. Wang, "Improved near-infrared ocean reflectance correction algorithm for satellite ocean color data processing," *Opt. Express*, vol. 22, no. 18, p. 21657, Sep. 2014, doi: 10.1364/OE.22.021657.

[39] J. E. O'Reilly *et al.*, "Ocean color chlorophyll a algorithms for SeaWiFS, OC2, and OC4: Version 4," in *SeaWiFS Postlaunch Calibration and Validation Analyses, Part 3*, vol. 11, S. B. Hooker and E. R. Fire-Stone, Eds. Greenbelt, MD, USA: NASA Goddard Space Flight Center, 2000, p. 49.

[40] P. J. Werdell, B. A. Franz, and S. W. Bailey, "Evaluation of shortwave infrared atmospheric correction for ocean color remote sensing of Chesapeake Bay," *Remote Sens. Environ.*, vol. 114, no. 10, pp. 2238–2247, Oct. 2010, doi: 10.1016/j.rse.2010.04.027.

[41] C. Goyens, C. Jamet, and K. G. Ruddick, "Spectral relationships for atmospheric correction II improving NASA's standard and MUMM near infra-red modeling schemes," *Opt. Express*, vol. 21, no. 18, Sep. 2013, Art. no. 21176, doi: 10.1364/OE.21.021176.

[42] Z. Xue, R. He, K. Fennel, W.-J. Cai, S. Lohrenz, and C. Hopkinson, "Modeling ocean circulation and biogeochemical variability in the gulf of Mexico," *Biogeosciences*, vol. 10, no. 11, pp. 7219–7234, Nov. 2013, doi: 10.5194/bg-10-7219-2013.

[43] N. N. Rabalais, R. E. Turner, and W. J. Wiseman, "Gulf of Mexico hypoxia: A.K.A. 'The dead zone,'" *Annu. Rev. Ecol. Syst.*, vol. 33, no. 1, pp. 235–263, Nov. 2002, doi: 10.1146/annurev.ecolsys.33.010802.150513.

[44] G. Zibordi, F. Melin, S. B. Hooker, D. D'Alimonte, and B. Holben, "An autonomous above-water system for the validation of ocean color radiance data," *IEEE Trans. Geosci. Remote Sens.*, vol. 42, no. 2, pp. 401–415, Feb. 2004, doi: 10.1109/TGRS.2003.821064.

[45] G. Zibordi *et al.*, "AERONET-OC: A network for the validation of ocean color primary products," *J. Atmos. Ocean. Technol.*, vol. 26, no. 8, pp. 1634–1651, Aug. 2009, doi: 10.1175/2009jtecho654.1.

[46] G. Chander *et al.*, "Applications of Spectral Band Adjustment Factors (SBAF) for cross-calibration," *IEEE Trans. Geosci. Remote Sens.*, vol. 51, no. 3, pp. 1267–1281, Mar. 2013, doi: 10.1109/TGRS.2012.2228007.

[47] P. J. Werdell and S. W. Bailey, "An improved *in-situ* bio-optical data set for ocean color algorithm development and satellite data product validation," *Remote Sens. Environ.*, vol. 98, no. 1, pp. 122–140, Sep. 2005.

[48] M. Wang and W. Shi, "Cloud masking for ocean color data processing in the coastal regions," *IEEE Trans. Geosci. Remote Sens.*, vol. 44, no. 11, pp. 3105–3196, Nov. 2006, doi: 10.1109/TGRS.2006.876293.

[49] S. W. Bailey and P. J. Werdell, "A multi-sensor approach for the on-orbit validation of ocean color satellite data products," *Remote Sens. Environ.*, vol. 102, nos. 1–2, pp. 12–23, May 2006.

[50] A. T. C. Broerse *et al.*, "The cause of bright waters in the Bering Sea in winter," *Continental Shelf Res.*, vol. 23, no. 16, pp. 1579–1596, Oct. 2003.

[51] T. Tyrrell and A. Merico, "*Emiliania huxleyi*: Bloom observations and the conditions that induce them," in *Coccolithophores: From Molecular Processes to Global Impact*, H.R. Thierstein and J. R. Young, Eds. New York, NY, USA: Springer-Verlag, 2004.

[52] S. Sathyendranath, Ed., *Phytoplankton Functional Types From Space*. Dartmouth, NS, Canada: IOCCG, 2014.

[53] S. Sathyendranath, Ed., *Remote Sensing of Ocean Colour in Coastal, and Other Optically-Complex, Waters*. Dartmouth, NS, Canada: IOCCG, 2000.

[54] D. Doxaran, J.-M. Froidefond, S. Lavender, and P. Castaing, "Spectral signature of highly turbid waters," *Remote Sens. Environ.*, vol. 81, no. 1, pp. 149–161, Jul. 2002, doi: 10.1016/s0034-4257(01)00341-8.

[55] T. S. Moore, M. D. Dowell, and B. A. Franz, "Detection of coccolithophore blooms in ocean color satellite imagery: A generalized approach for use with multiple sensors," *Remote Sens. Environ.*, vol. 117, pp. 249–263, Feb. 2012, doi: 10.1016/j.rse.2011.10.001.

[56] N. D. Walker and B. H. Adele, "Impacts of winter storms on circulation and sediment transport: Atchafalaya-Vermilion Bay Region, Louisiana, U.S.A," *J. Coastal Res.*, vol. 16, no. 4, pp. 996–1010, 2000.

[57] E. J. D'Sa, R. L. Miller, and B. A. McKee, "Suspended particulate matter dynamics in coastal waters from ocean color: Application to the northern Gulf of Mexico," *Geophys. Res. Lett.*, vol. 34, Dec. 2007, Art. no. L23611, doi: 10.1029/2007GL031192.

[58] G. W. Stone, D. A. Pepper, J. Xu, and X. Zhang, "Ship shoal as a prospective borrow site for barrier Island restoration, Coastal South-Central Louisiana, USA: Numerical wave modeling and field measurements of hydrodynamics and sediment transport," *J. Coastal Res.*, vol. 201, pp. 70–88, Jan. 2004.

[59] P. Naik, E. J. D'Sa, M. Grippo, R. Condrey, and J. Fleeger, "Absorption properties of shoal-dominated waters in the Atchafalaya Shelf, Louisiana, USA," *Int. J. Remote Sens.*, vol. 32, no. 15, pp. 4383–4406, Aug. 2011, doi: 10.1080/01431161.2010.486807.

[60] W. Shi and M. Wang, "Satellite observations of flood-driven Mississippi River plume in the spring of 2008," *Geophys. Res. Lett.*, vol. 36, Apr. 2009, Art. no. L07607, doi: 10.1029/2009GL037210.

[61] I. Joshi and E. D'Sa, "Seasonal variation of colored dissolved organic matter in Barataria Bay, Louisiana, using combined landsat and field data," *Remote Sens.*, vol. 7, no. 9, pp. 12478–12502, Sep. 2015.

[62] V. Vantrepotte, H. Loisel, D. Dessailly, and X. Mériaux, "Optical classification of contrasted coastal waters," *Remote Sens. Environ.*, vol. 123, pp. 306–323, Aug. 2012, doi: 10.1016/j.rse.2012.03.004.

[63] E. J. D'Sa, R. L. Miller, and C. D. Castillo, "Bio-optical properties and ocean color algorithms for coastal waters influenced by the Mississippi River during a cold front," *Appl. Opt.*, vol. 45, no. 28, p. 7410, Oct. 2006, doi: 10.1364/AO.45.007410.

[64] E. J. D'Sa, I. D. Joshi, B. Liu, D. S. Ko, C. L. Osburn, and T. S. Bianchi, "Biogeochemical response of Apalachicola Bay and the shelf waters to Hurricane Michael using ocean color semi-analytic/inversion and hydrodynamic models," *Front. Mar. Sci.*, vol. 6, no. 523, Aug. 2019, doi: 10.3389/fmars.2019.00523.

Ishan D. Joshi received the M.Tech. degree in earth system science and technology from IIT Kharagpur, Kharagpur, India, in 2011 and the Ph.D. degree in oceanography from Louisiana State University, Baton Rouge, LA, USA, in 2017.

He is currently a Post-Doctoral Researcher with the Scripps Institution of Oceanography, University of California at San Diego, San Diego, CA, USA. His research interests include ocean color remote sensing, satellite oceanography, and machine learning.

Dr. Joshi was a recipient of the German Academic Exchange Service (DAAD) Award, Germany, and the Ministry of Human Resource and Development Scholarship, India, during his M.Tech. Program.

Eurico J. D'Sa received the M.S. degree in electrical engineering from the Indian Institute of Sciences, Bengaluru, India, in 1990, and the Ph.D. degree in marine sciences from The University of Southern Mississippi, Hattiesburg, MS, USA, in 1996.

He joined the Department of Oceanography and Coastal Sciences, Louisiana State University, Baton Rouge, LA, USA, in 2004, where he is currently a Professor. His research interests are in ocean color remote sensing, bio-optical properties of coastal and ocean waters, physical–biogeochemical interactions, and the study of coastal biogeochemical processes using field and satellite data.